DEVELOPMENT OF A CONSTITUTIVE MODEL PREDICTING THE POINT OF SHORT-CIRCUIT WITHIN LITHIUM-ION BATTERY CELLS

By
JOHN EARL CAMPBELL, JR

B.S. Chemistry
United States Naval Academy, 1995

M.S.E. Engineering Management
Catholic University of America, 2002

Submitted to the
DEPARTMENT OF MECHANICAL ENGINEERING

In Partial Fulfillment of the Degrees of

NAVAL ENGINEER
and
MASTER OF SCIENCE IN MECHANICAL ENGINEERING

at the
MASSACHUSETTS INSTITUTE OF TECHNOLOGY
June, 2012

Signature of Author: _____
Department of Mechanical Engineering
May 9, 2012

Certified By: _____
Tomasz Wierzbicki
Professor of Applied Mechanics
Thesis Supervisor

Accepted By: _____
David E. Hardt
Ralph E. and Eloise F. Cross Professor of Mechanical Engineering
Chair, Department Committee on Graduate Students

Development of a Constitutive Model Defining the Point of Short-Circuit Within Lithium-Ion Battery Cells

By

John Earl Campbell Jr.

Abstract

The use of Lithium Ion batteries continues to grow in electronic devices, the automotive industry in hybrid and electric vehicles, as well as marine applications. Such batteries are the current best for these applications because of their power density and cyclic life. The United States Navy and the automotive industries have a keen interest in making and maintaining these batteries safe for use within the public. The testing necessary to ensure this safety is time consuming and expensive to manufacturers, thus a constitutive model that can emulate the effects of mechanical abuse to a battery cell or pack is necessary to be able to rapidly test various configurations and enclosures to preclude possible short circuit and thermal runaway of an installed battery is necessary. Homogenized computational cells have been developed at the MIT Crashworthiness Laboratory and this research validates and refines those models for use in future work with both cylindrical and prismatic cells.

A total of 22 mechanical abuse tests were conducted on partially charged cylindrical and pouch/prismatic Li-Ion cells under multiple loading conditions. The tests included lateral compression by cylindrical rods of various sizes, three point bending tests, and hemispherical punch tests on cylindrical cells. For the pouch/prismatic cells, the tests included hemispherical punch tests of various sizes as well as a conical punch test, vertical cylindrical punch test, and rectangular punch test. The tests measured the force imparted to the cell, linear displacement of the punch into the cell structure, voltage output of the cell, as well as the temperature at the surface of the cell.

The test data was utilized to validate and refine homogenous computational models for both cylindrical and pouch/prismatic Li-Ion cells for future use in the MIT Crashworthiness Laboratory. The computational models subjected to simulated tests that were conducted on actual cells in the laboratory conclude that the computational models are valid and behave well compared to actual cells.

This paper reports on results generated for the Li-Ion Battery Consortium at MIT.

Thesis Supervisor: Tomasz Wierzbicki
Title: Professor of Structural Mechanics

Table of Contents

List of Figures

List of Tables

List of Equations

Acknowledgements

The author thanks the following individuals for their assistance in completing this thesis:

Professor Tomasz Wierzbicki for his direction, guidance, and wisdom on this project. His expertise is fundamental to the continued success of the Li-Ion Battery Consortium at MIT.

Dr. Elham Sahraei for her collaborative efforts in writing, assembling, and publishing three academic papers from which this thesis is derived. Her expert analytical capability along with her detailed Finite Element Analysis continues to form the backbone of the work for the Li-Ion Battery Consortium at MIT.

CAPT Mark Welsh and CAPT Mark Thomas for their leadership of the 2N program during these three years at MIT.

1. Introduction and Overview of Lithium-Ion Battery Literature

Technology has created a vast need for rechargeable sources of power. People use small electronic devices on a daily basis from cell phones to laptop computers to hybrid or electric vehicles. Because of the increases in the use of rechargeable power sources the science of battery storage has evolved accordingly. Manufacturers continue to try and find newer and better ways to store energy while maintaining affordability and compactness.

Lithium-ion batteries are best suited to the portable electronic world because of a high power density, low weight, faster charge time, and long cell life Raman, N.S. et al(2002) (1). They also have the advantage of being maintenance free and a sealed integrity resulting in no off-gassing. The drawback to the lithium-ion battery technology is the potentially catastrophic failure of the battery under abusive conditions. These abusive conditions can result from rapid charge and discharge rates without limitations, thermal stresses from the environment, and mechanical abuse from impact or damage.

In order to mitigate the potential for catastrophic failure in the lithium-ion battery, there are mechanisms and means available to manufacturers. These means include variations in internal chemistry, cell construction, passive and active safety mechanisms, as well as cell joining technologies and battery pack arrangement Fischetti, M(2010) (2). The latter focuses more on larger hybrid and electric vehicle (HEV) batteries.

Additionally, the U.S. Navy continues to maintain a keen interest in the development of safe lithium-ion battery technologies for use in all aspects of their efforts. The Navy has developed

Technical Manuals detailing the approval process, testing, and risk assessment (3) (4). It is desired that use of lithium-ion batteries can be used on naval vessels in the future.

Battery Cell Chemistry and Construction

Internal battery cell chemistries and construction are typically proprietary by the manufacturer, but there are some common characteristics to the cells in question. This paper addresses testing on both cylindrical, or jelly roll cells, as well as pouch, or prismatic cells. Construction of both types of cells is reviewed. Overall chemistries of the cells can be common to either construction technique. No specific differentiation is provided.

Battery cell chemistry impacts storage capacity, peak voltage, and activity of the cell. Because activity of the cell has a direct impact on the safety of the cell, the chemistry is addressed from this point of view. Figure 1, shown below, outlines the intercalation compounds commonly used in the anodic end of Li-ion batteries as described in Juzkow, Marc W., et al (1997) (5). The progression up the chain from Li metal, at 0 eV, to LiF, at 6 eV, increases in both activity, and storage capacity. As activity increases, the thermal stability of the cell decreases as shown in Juzkow, Marc W., et al (1997) (6). Because both are increasing at the same time, a balance must be struck between storage capacity and thermal stability.

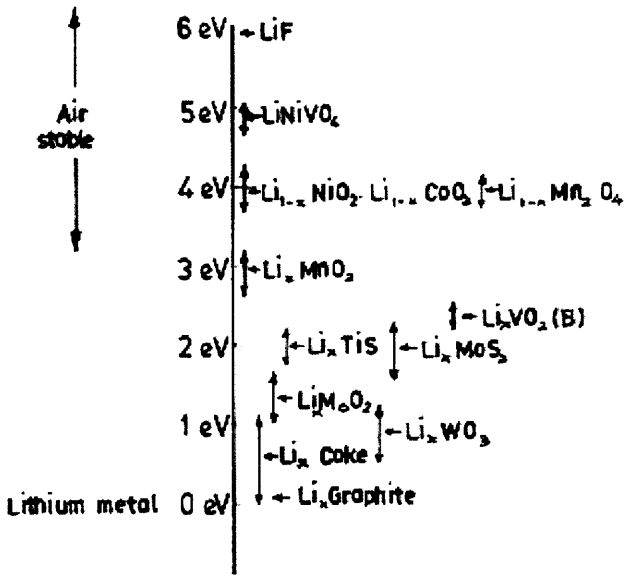

Figure 1: Lithium Intercalation Compounds (5)

The most common anodic chemistries are $LiNiO_2$, $LiCoO_2$, and $LiMnO_2$. It is considered that the most thermally stable intercalating compound in use is $LiMnO_2$, but its power density is significantly lower. Both the cylindrical and prismatic cells tested were $LiCoO_2$ chemistry.

Construction for each type of cell is similar in nature, but it can be seen in Figure 2 that the pouch cell is a layered construction whereas the cylindrical cell is a rolled construction. Because the chemistries of both cell types tested are the same, the separator, anode, and cathode layers are the same.

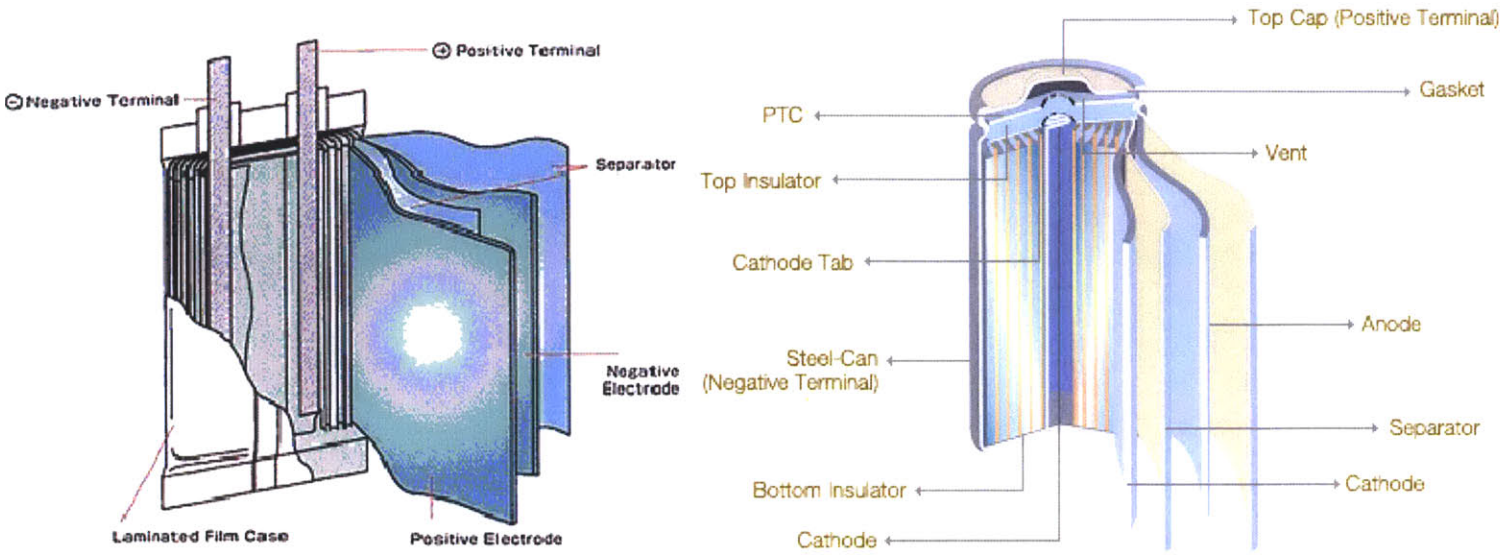

Figure 2: Pouch and Cylindrical Cell Construction (7)

The anode consists of a thin sheet of aluminum with the $LiCoO_2$ layered on both sides. The cathode consists of a thin copper sheet with powdered graphite layered on one side. The copper and aluminum sheets act as the current collectors. An organic electrolyte is contained between each layer allowing the migration of Li ions through the separator. The separator is a thin polyolefin layer, typically polypropylene or polyethylene. The separator keeps the anodic and cathodic layers from touching. An internal short-circuit is expected to be as a result of a breakdown of the separator layer, thus the strength of the separator, as evaluated in Sheidaei, Azadeh, et al(2011) (8), is critical to keeping the anode and cathode from coming in contact with one another.

Cell Joining Technologies

In evaluating Figure 2, it can be seen that there are both spot welds and laser welds are used in the construction of the individual cylindrical cell. When constructing larger battery modules and packs, several technologies are available for use. The advantages and disadvantages of joining

processes in battery manufacturing, to include resistance welding, laser welding, ultrasonic welding, and mechanical joining are detailed in Shawn Lee, S., et al(2010) (9).

Several cells are joined together to form battery modules and several modules are joined together to form a battery pack. The manner in which the joining takes place affects the overall safety and reliability of the battery pack. As also stated in Shawn Lee, S., et al(2010) (9), regardless of the joining technology used, robust joints must be developed to combat against fatigues and corrosion for long life are needed for battery manufacturing.

Failure Analysis

The catastrophic failure of a lithium-ion battery could result in a thermal runaway condition following an internal short-circuit. Because an internal short-circuit causes a rapid (almost instantaneous) release of energy stored in the cell, the state of charge (SOC) of the cell determines the outcome. Wang, Quingsong et al(2010) developed a swallowtail catastrophe potential function to predict when a thermal runaway condition could result (10). So long as the battery is operated outside the predicted thermal runaway conditions, the battery is safe. Because there is never a 100% guarantee of operation within those boundaries, catastrophic events will occur.

Following a catastrophic incident involving one cell or multiple cells, an analysis of the event is undertaken. In Swart, J., et al (2008), it is shown that a proven methodology for incident investigations involving lithium ion battery systems has been developed (11). The methodology utilizes a decision tree matrix with a carefully executed investigation and assessments of the information gathered. From the aforementioned methodology, recommendations regarding

battery component safety, as well as incorporation of improvements to passive and active safety mechanisms can be proffered to manufacturers to ensure the consumer is safe.

Passive and Active Safety Mechanisms

The construction of a battery pack begins with the cell. The safety of the battery pack also begins with the cell. Once cellular chemistry, pack arrangement, and joining processes are determined, then the only remaining variables under the manufacturer's control for safety of the battery pack is the design and installation of passive and/or active safety mechanisms. The use of various safety mechanisms is detailed in Balakrishnan, P.G., et al(2006) and is summarized below (12).

Safety vents are utilized as a backup safety device to relieve overpressure conditions in the event of an overcharge or rapid discharge. Because this mechanism opens the cell's internal structure to the environment and allows electrolyte to escape, it is considered a backup device and is passive in nature.

Thermal fuses have been used in circuit breaker technology for years and the same technology applies to battery construction to limit current. Because thermal fuses are typically an alloyed fusible link, they are a one-shot and permanently open a circuit. These devices are cheap passive current limiters that can open an individual cell in the event of an overcurrent situation prior to a thermal runaway event.

Additionally, other circuit breakers in the form of magnetic switches, thermistors, and bi-metallic strips would open in an over-temperature condition without the requirement to replace components. Because the aforementioned devices can be volume consuming and expensive to

install, positive temperature coefficient devices were developed to limit current flow by increasing resistance as temperature increases. These devices are a self-limiting component, inexpensive to install, consume little space, and are strictly passive in nature.

Electronic protective circuits preventing inadvertent overcharging and over-discharging of battery cells have been installed in lithium-ion batteries for several years now and testing done by Tobishima, S., et al(2000) (13) shows that the current limiting devices help to protect active cells and increase the margin of safety specifically in $LiCoO_2$ cells.

Considering the use of lithium-ion batteries in HEV and EV vehicles, both Tesla Motors and General Motors have instituted several active and passive mechanisms into the construction of the battery packs for use in their vehicles. Berdichevsky, G., et al(2006) (14) and Guerin, J.T., et al(2009) (15) detail the open source information regarding safety mechanisms installed in both the Tesla Roadster and the Chevy Volt.

The Tesla Roadster incorporates several of the aforementioned passive safety devices. In addition to those, the Roadster incorporates a passive aluminum battery enclosure vice plastic to improve crash response and cooling coils to remove generated heat from both charging and discharging. Actively, the Roadster battery pack contains multiple microprocessors the continually monitor voltage, current, and temperature, as well as sensors to monitor accelerations from a crash or rollover, smoke, humidity, and moisture. When this active system detects a parameter outside a specified range, the high voltage power supply is immediately disconnected from the vehicle.

General Motors evaluated the crashworthiness and safety of the vehicle and battery pack by initially establishing the location of the battery pack within the vehicle, then subsequently

evaluating the kinematics of how the vehicle is affected on impact. An electronics monitoring system is also installed to monitor the health of the vehicle and battery. The system monitors at a 1MHz rate and is OBD-II compliant.

2. Description of Equipment and Setup For Testing Program

The experiments were designed to measure not only the load displacement relation of the punch, but also the voltage output of the battery, as well as a possible temperature rise. The following sections outline all of the equipment and software utilized during the testing of the cylindrical and pouch lithium-ion cells.

Battery Discharge Box

A resistance box was constructed to discharge the 18650 cylindrical Li-Ion cells from an approximate 50% charge (3.83V) to an approximate 10% charge (3.600V). The discharge rate was established at approximately 0.2C. Because the resistance is constant over the discharge range and voltage is changing as the battery discharges, the current also drops in accordance with Ohm's Law shown in Equation 1. As the battery discharge progressed, voltage was monitored until reaching 3.600V or approximately 90% discharged as shown in Figure 3. Because the cylindrical cells are rated at 2200mAh at full charge, the batteries were discharged as a safety precaution to minimize the possibility of thermal runaway upon short circuit.

$$I = \frac{E}{R} \; ; \; where\ I\ is\ Current\ in\ Amps, E\ is\ Voltage\ in\ Volts, and\ R\ is\ Resistance\ in\ Ohms$$

Equation 1: Ohm's Law

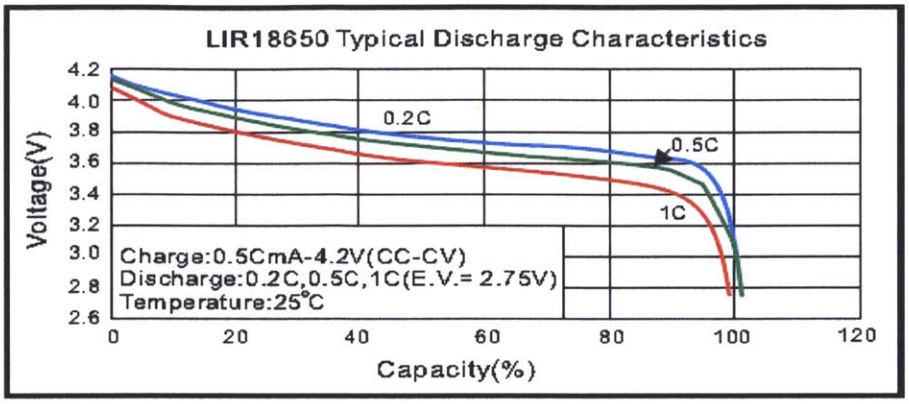

Figure 3: 18650 Discharge Characteristics

The box, shown in Figure 4, was constructed using commercial-off-the-shelf parts and the parts listing is in Table 1. There are two values of resistance that can be established, based on the state of charge of the battery, by flipping the right switch, as shown in Figure 4. These values, as measured following construction are 8.2 Ohms and 8.8 Ohms respectively. A schematic of the internals is shown in Figure 5. The box was assembled to maximize heat dissipation by the resistance elements.

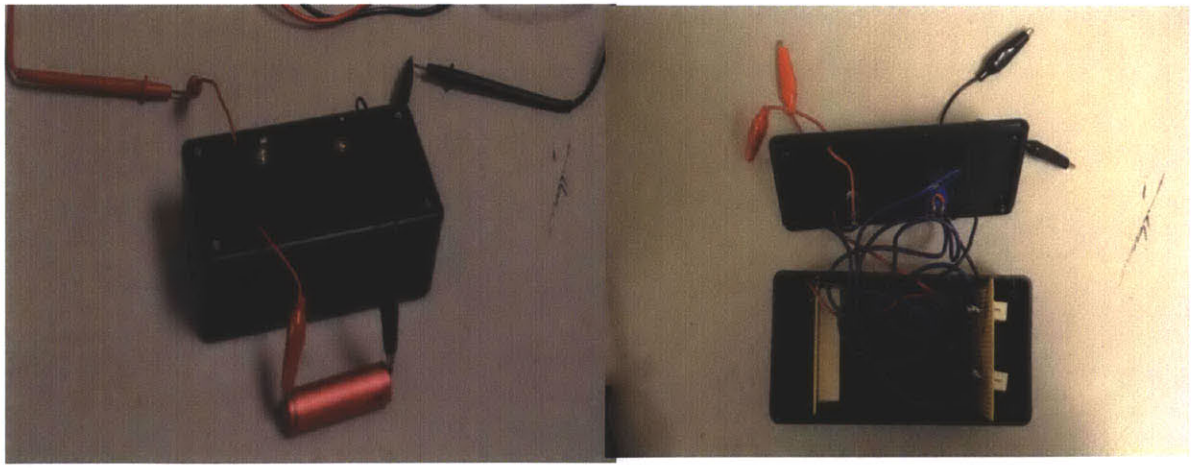

Figure 4: Battery Discharge Box

Part Number	Description
#276-1396	(1) Pre-Punched Perfboard
#271-120	(2) 20W 8-Ohm Non-Inductive Resistor 5%
#55050262	(3) 25W Cermet Power Wirewound Resistor 0.47 Ohm 5%
#275-614	(4) DPDT Submini Toggle Switch
#275-612	(5) SPST Submini Toggle Switch
#278-1156	(6) 14" Insulated Test/Jumper Leads
#270-1806	(7) Project Enclosure (6x4x2")

Table 1: Discharge Box Parts List

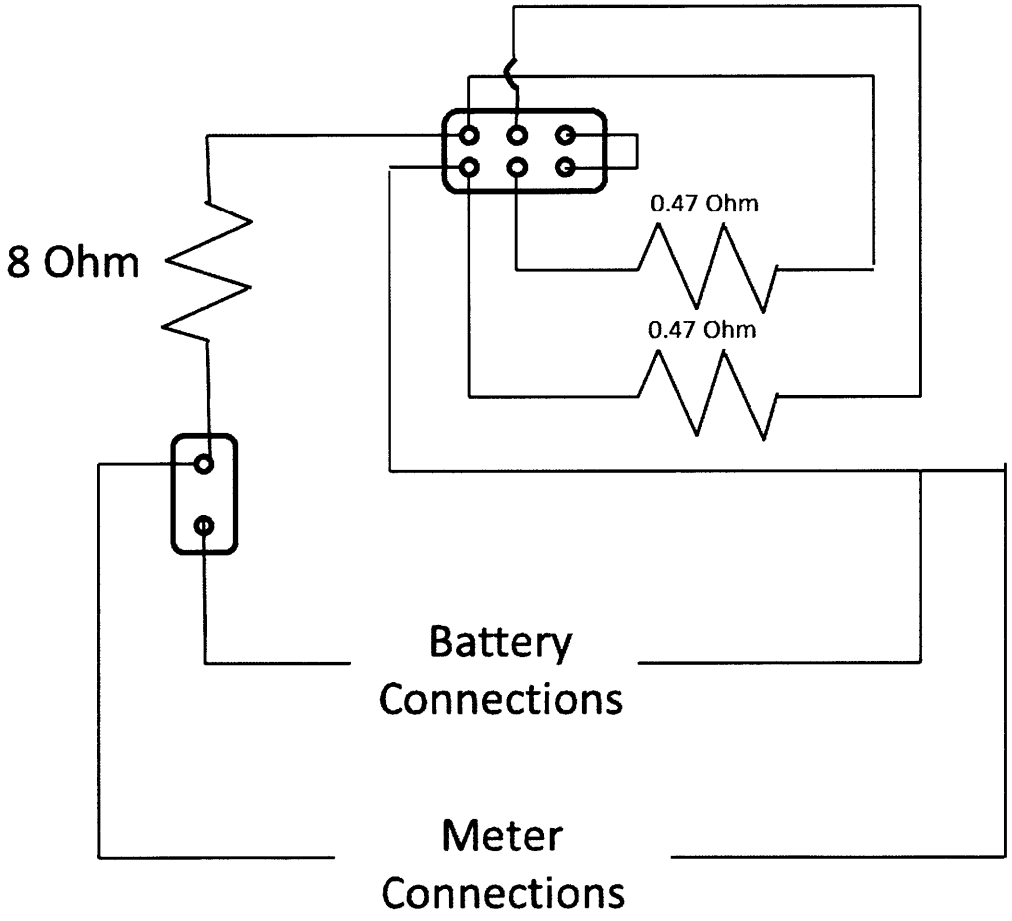

Figure 5: Discharge Box Schematic

Because battery state of charge (SOC) is extremely difficult to predict as identified in Sun, Fengchun et al(2011) (16), and not the purpose of this research, a simplified mechanism was used to monitor the SOC of the cells to be tested. Loaded voltage is monitored by connecting a

voltmeter to the upper two alligator clips. Once the final voltage is reached, based on state of discharge and discharge rate, the left switch is turned off, and the battery is disconnected. Loaded voltage and static voltage will differ because of the chemical reaction occurring internal to the battery. The battery is allowed to return to room temperature and the chemical reaction to reach equilibrium prior to checking no-load voltage. If no-load voltage is above the SOC desired for testing, then the cell is discharged further.

Ventilation Chamber

A ventilation chamber was constructed using 0.25" thick acrylic sheets on an extruded aluminum frame. A 4" diameter ventilation duct was attached to the back of the box to provide a net negative airflow. The fan has the capability to move 135 SCFM of air through a 4" opening. Flow was limited through the box using spacers at the bottom of the front as shown in the close up in Figure 6. The net effect was to remove any evolved gasses from the battery electrolyte when crushed and prevent inhalation of those gasses.

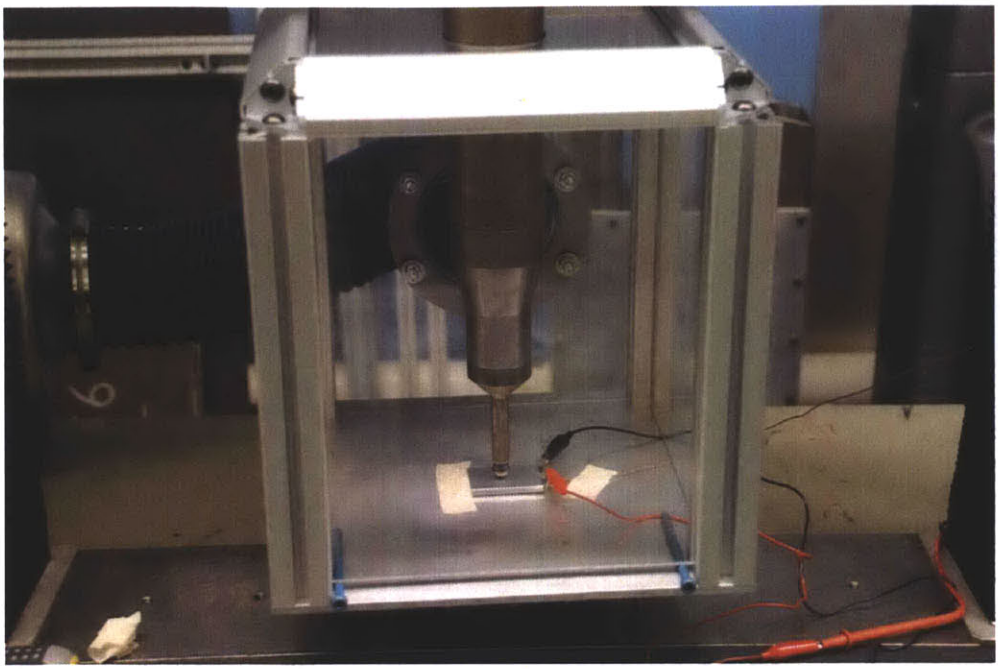

Figure 6: Close up of Test Setup

MTS Loading Frame

All tests were performed on the displacement controlled 200 KN machine equipped with a 10KN load cell. The cross head speed is in the range of 0.1mm/min to 1000mm/min with deflection accuracy of 1%. A calibrated load cell with the capacity to measure up to 10 KN or 200 KN in compression was used for measuring the applied load in the tests. Each load cell has an accuracy level of 1% of the measured load. A steel extension rod from the load cell to the hemispherical punches and horizontal rods was used to provide connectivity through the ventilation box boundary. The overall setup is shown in Figure 7.

The MTS software, Testworks 4, was configured for the attached load cell and a linear extension rate of 1mm per minute was used during the tests. The system was also configured to automatically stop the test in the event of extension to the base plate, or if load exceeded the

capacity of the attached load cell. The displacement of the cross head and measured force applied to the load cell was recorded vs. time at a sampling rate of 1Hz.

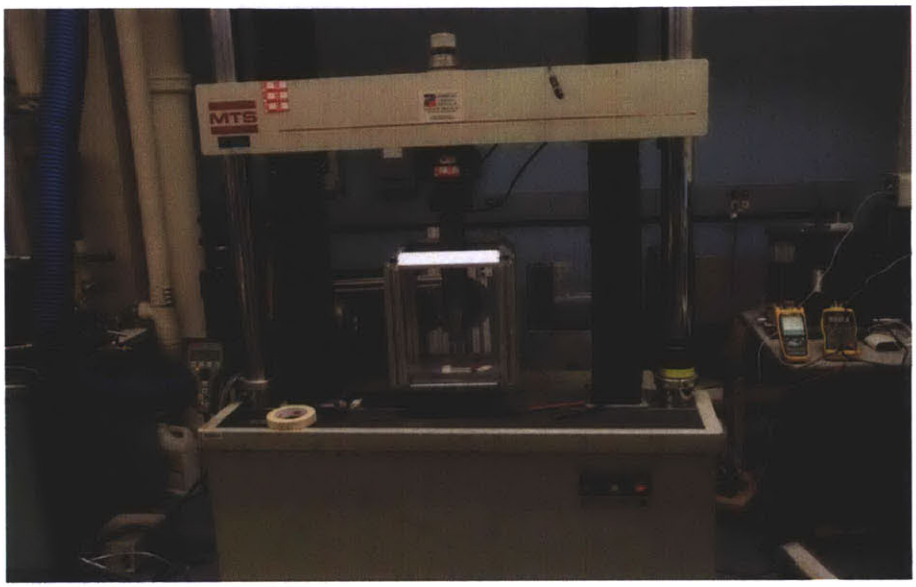

Figure 7: MTS Test Setup

Voltmeter

A Radio Shack 46 Range Digital Multimeter, shown in Figure 8, was used to measure voltage of the batteries during the tests. The voltmeter is equipped with an RS-232 digital output and was connected to the MTS computer via a COM port. The meter has an accuracy of +/- 0.3% from 0-4V. The supplied Meterview software was used to record the voltage output of the battery vs. time. The software recorded the data at a rate of 1Hz.

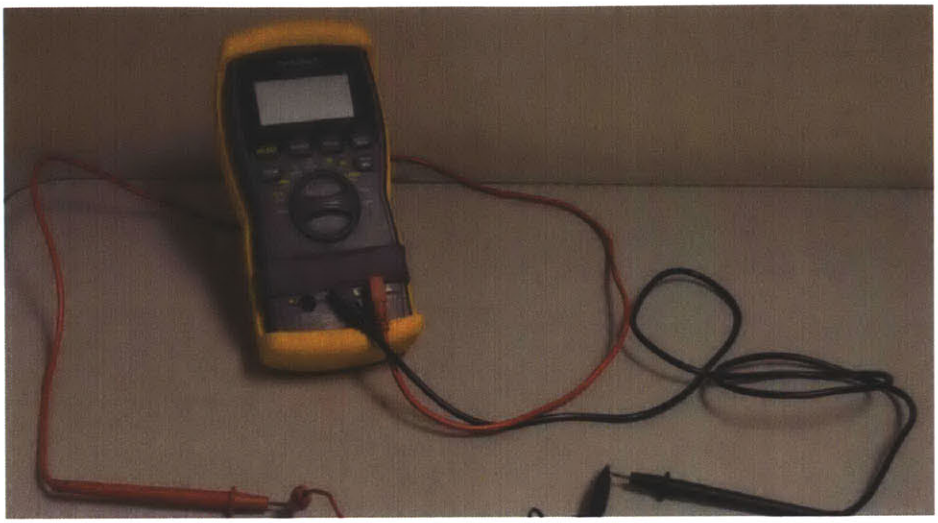

Figure 8: Radio Shack Multi-meter

Thermometer

The Omega HH176 thermometer with a style II CO-2-K thermocouple was used to measure surface temperature of the batteries during the tests and is shown in Figure 9. The HH176 measurement device was connected to the MTS computer via a USB cable to record temperature readings. The HH176 has an accuracy level of +/- 0.05% of indicated reading. The thermocouple is constructed of proprietary Chromega-Alomega materials at 0.0005" thick, has a response time of 2-5 ms and a maximum temperature of 540 C. The thermocouple was mounted on the underside of the battery to minimize interaction with the cooling effect of the ventilation box. The supplied software, Temp Monitor, recorded the temperature data vs. time at a rate of 1Hz.

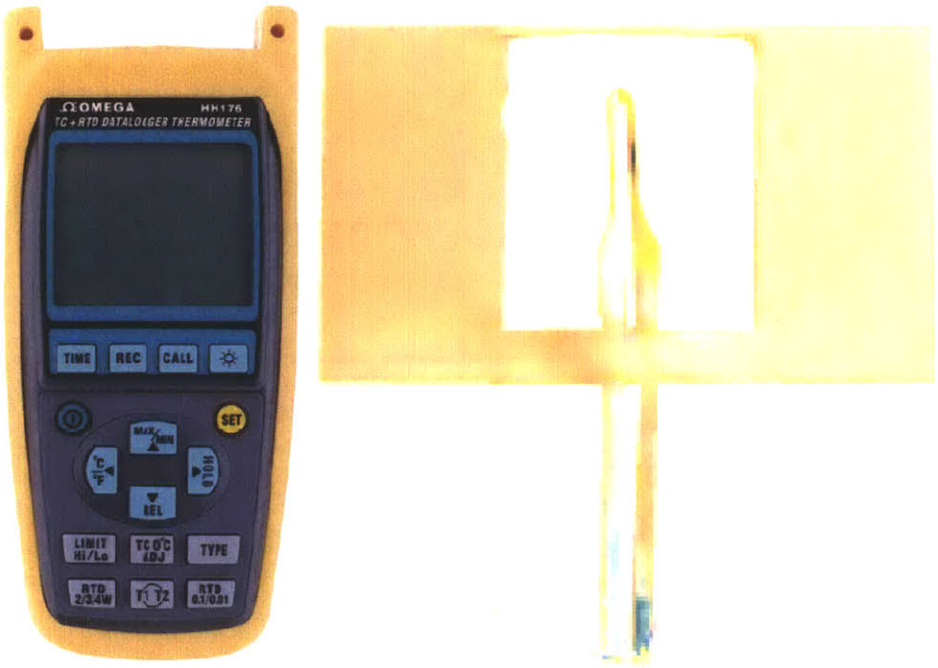

Figure 9: Omega Thermometer and Thermocouple

Software Integration

Because each piece of software operated independently without a synced time source, measures were put into place to ensure manual syncing of recorded data to within 1 second. There were three separate outputs of the test, force-displacement, voltage, and temperature. Each of the data streams was recorded within the respective software packages and saved in a delimited text file format. These files were imported into Microsoft Excel and the results plotted and shown below in the results section. A screen capture interface between these three channels, shown in Figure 10, was used to manually manipulate the data streams to ensure a common, normalized zero point for data recording and plotting.

Testworks Software
Force and
Displacement

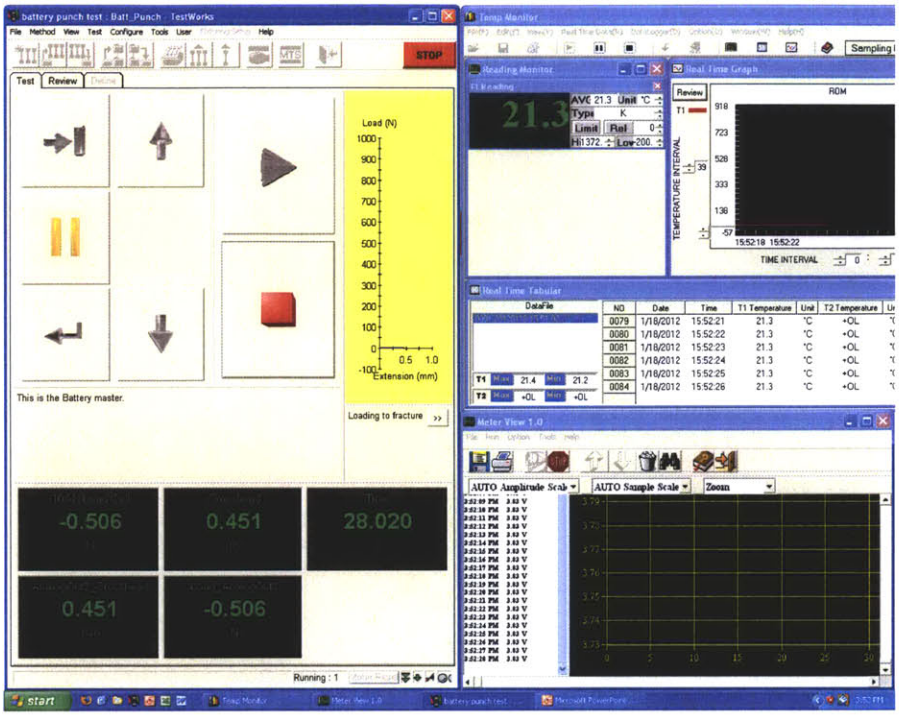

Temp Monitor
Temperature

Meterview
Software

Figure 10: Normalization of Test Data

3. Description of the Testing Program on 18650 Cylindrical Cells

A series of tests was conducted on cylindrical lithium ion batteries. The cells chosen for these tests were 18650 cells and used lithium cobalt dioxide chemistry. The 18650 is a standard designation for cylindrical cells that are 18mm in diameter and 65mm in length. The cells were procured at approximately 50% SOC and were discharged using the battery box in Section 2 to a point approximately 90% discharged, or 10% SOC. Because these cells have a capacity of 2600mAh, the risk of thermal runaway is much greater if the cells were allowed to remain at 50% SOC. The specifications for the cylindrical cells used in this test are shown in Table 2: Specifications of 18650 cells.

Table 2: Specifications of 18650 cells

Norminal Capacity	2600mAh
Size	65mm x 18mm x 18mm
Weight(Typical)	45 g
Charge Method	Constant Current and Constant Voltage(4.2V)
Nominal Voltage	3.7 V
Max. Charge Current	1CmA(2600mA)
Max. Disharge Current	2CmA(5200mA)
Discharge Temperature	-20°C ~ +60°C
Energy Density	565Wh/I, 215Wh/kg
Charging Time	3hrs(Standard) or 2.5hrs(Rapid)

The tests that were conducted on the 18650 cells follow:

- 90 degree lateral indentation test using a 0.625 inch (15.9mm) rod
- 0.5 inch (12.7mm) hemispherical punch test
- Three-point bending test

Lateral Indentation of the Cell by a Rigid Rod

A cylindrical rod with radius of 8 mm was attached to the restraining block (see Figure 11) and load cell of the loading frame with a constant velocity of 1.0 mm/min. Figure 12 (left) shows the

measured force and displacement variation over time for the test performed on the 18650 cylindrical battery. The peak force and associated displacements for the test were 6469 N, and 6.3 mm. Figure 12 also shows the point of short circuit in the cell, as detected by a drop in force and voltage, as well as an increase in temperature. One can see from these figures that the peak force and drop in voltage occurs almost simultaneously, which confirms the occurrence of short circuit. The deformed battery is shown in Figure 12(right). The battery is tightly wrapped around the rigid rod.

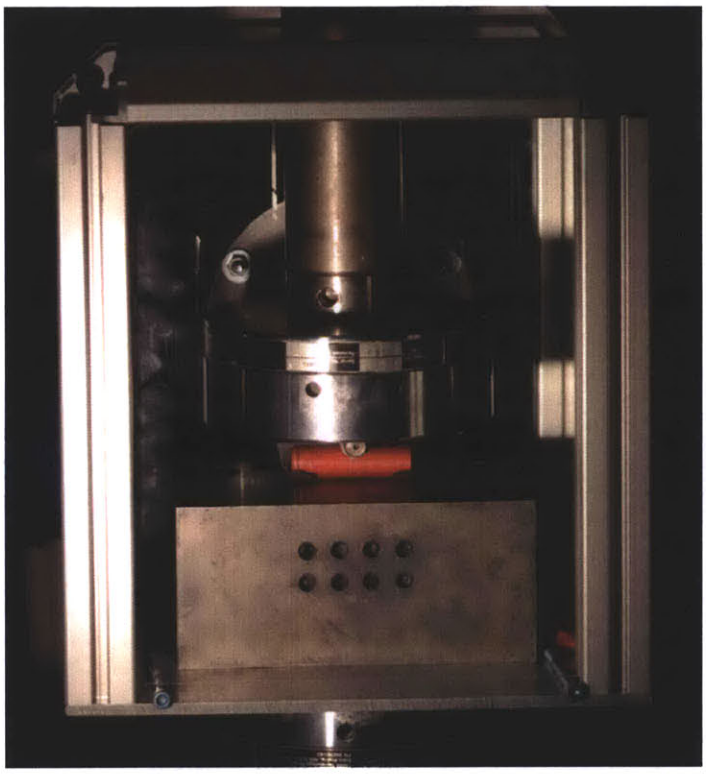

Figure 11: Lateral Indentation Setup

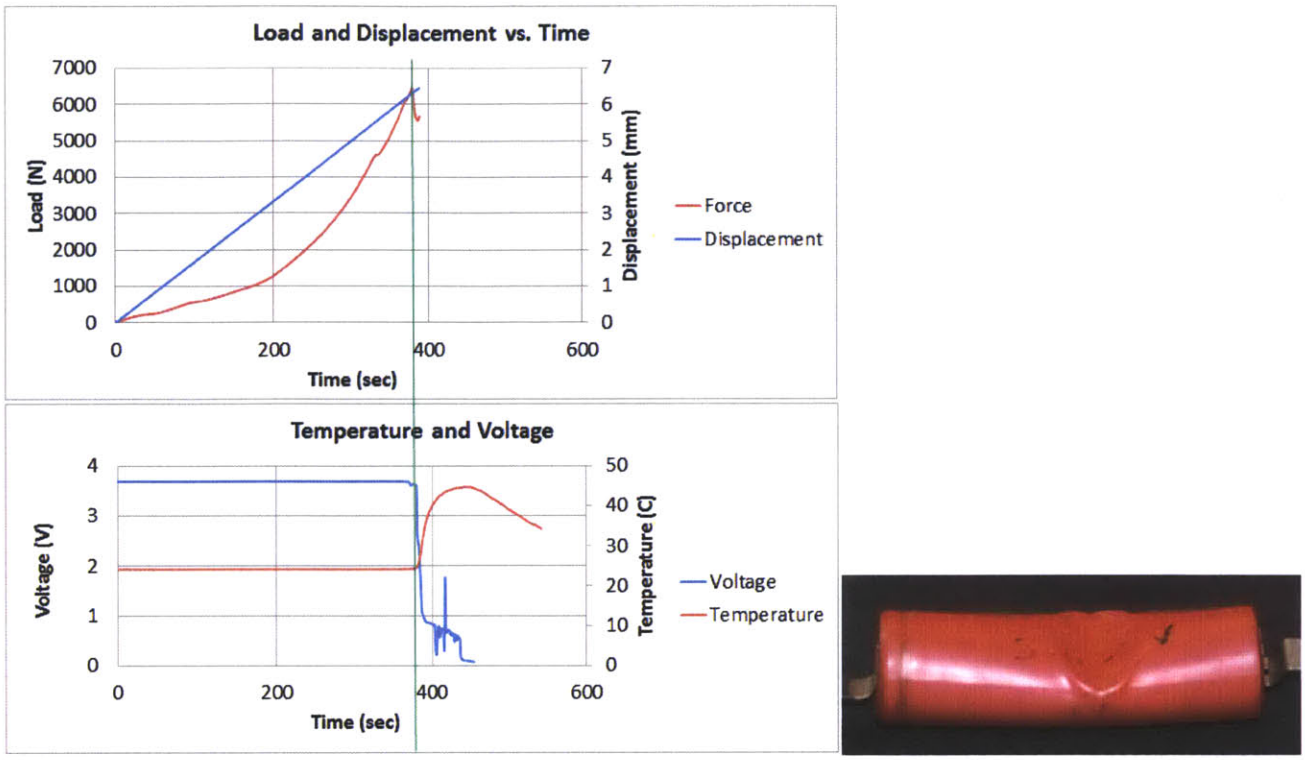

Figure 12: Detecting the Point of Short Circuit in Rod Indentation Test from Force, Voltage, and Temperature Measurement (Left), and Deformed Shape of the Cell (Right)

Hemispherical Punch Test

In this test, the 18650 cell was crushed by a hemispherical punch of 12.7 mm diameter. Careful set up and measurement was used to make sure the center of the punch and cell were aligned, so that the cell will not slide under this loading scenario. The discharging procedure, and the details of instruments used to perform this test were similar to the previous test explained above. The set-up of this test is shown in Figure 13. This test and previous one would apply compressive stresses in the radial direction and tensile stresses in axial direction (in local coordinate system) under the punch. The difference between this test and the previous one is the tensile stresses could be applied both in axial and cross sectional elements, while in previous test, tensile stresses could only be developed in axial direction.

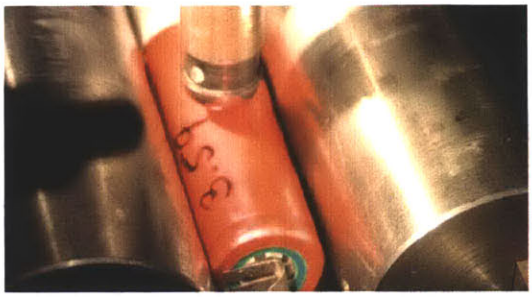

Figure 13: Crush Test of the 18650 Cell by a Hemispherical Punch

The variation of the force, displacement, voltage, and temperature versus time is shown in Figure 14. Again, it is seen that drop in the resisting force occurs at the same time as the drop in voltage. It is also observed that temperature starts to rise over a period of a minute and a half and falls back, which indicates release of the residual energy stored in the discharged cell. It will be shown in Section 5 that the short circuit occurs under the punch, which is far from the location of the temperature probe. The release of the heat around the point of short circuit should be much faster, and leading to larger temperatures. The present test could be of a value to research teams modeling thermal effects in abuse scenarios, see for example Sponitza, et al(2009) (17) and Shriram(2009) (18)

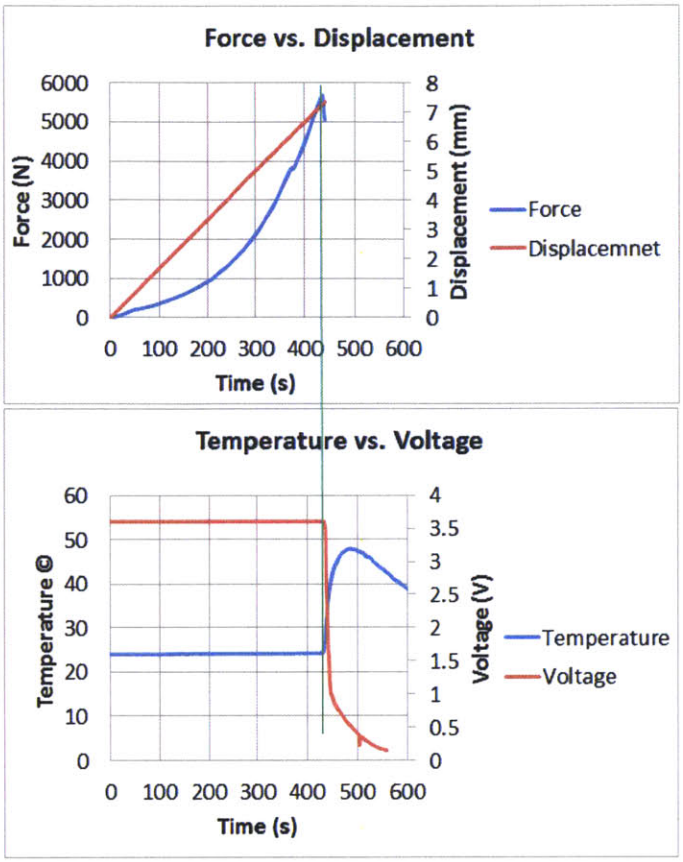

Figure 14: Detecting the Point of Short Circuit in Hemispherical Pun ch Crush Test from Force, Voltage, and Temperature Measurement

Three-point Bending Test

In addition to indentation and crush test performed to study the point of short circuit of the 18650 cells, a three point-bending test was performed. The bending loading of cylindrical cells could actually occur as a result of a complex interaction of cells inside a module during a severe crash. The state of stress in the bending test is a combination of global stresses resulting from bending of a short beam, as well as local stresses under the punch. Figure 15 shows the test set-up. The radius of the cylindrical indenter was 10 mm, and the radii of supporting cylinders were 24 mm.

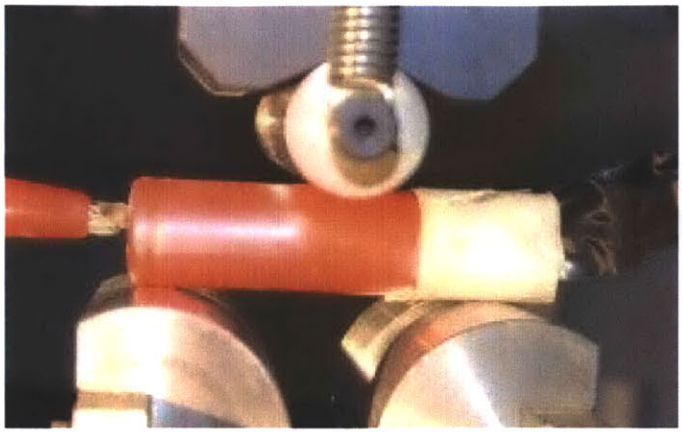

Figure 15: Three-point Bending Test Set-up

An interesting observation from this test was the relatively low ductility of the shell casing. It was observed that before a short circuit in the jellyroll was detected, a crack developed in the tensile side of the shell casing, which resulted in leakage of electrolyte from steel casing into the plastic wrap. This can be seen from the sequence of snapshots of the bending test shown in Figure 16. Fracture of shell casing initiated at t=350s, corresponding to punch displacement of 6.5 mm, see Figure 17. The crack propagates quite far, almost tow third of the diameter of the cell. The fracture of shell casing must have accelerated the onset of electric short-circuit. This effect can be easily prevented at the design stage, by making the shell casing from a more ductile material, such as stainless steel.

Figure 16: Development of Crack and Leaking Electrolyte in the Lower Side of the Cell under Tensile Loading

All the measured parameters of the cell response are shown in Figure 17. One can see that initially there is a linear response suggesting that the cell (combination of shell casing and jelly-roll) is behaving in a linear elastic range.

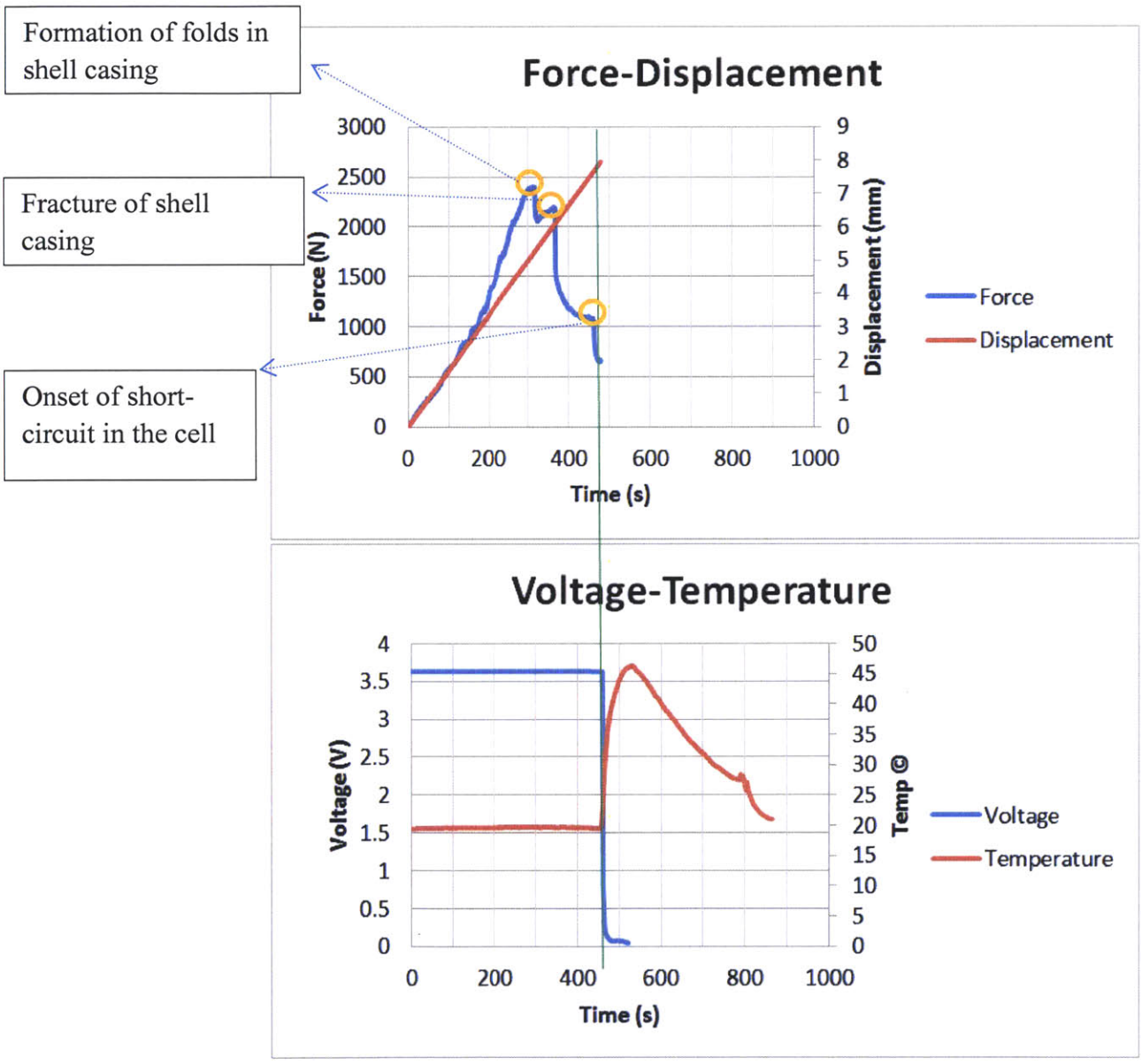

Figure 17: Force, displacement, voltage, and temperature measurements during three-point bending test

On the load-time diagram, one can distinguish three local peaks. The first peak corresponds to formation of small folds on the thin metal shell, causing a local drop in the force, and then the force level rises slightly, only to produce tensile fracture of the shell casing. It takes approximately another one millimeter of punch travel to initiate short circuit. Clearly, the jelly roll must have fractured internally. The precise location of the fracture zone could be determined by a CT-Scan.

4. Description of the Testing Program on Pouch/Prismatic Cells

Commercially available lithium–polymer pouch batteries with lithium cobalt dioxide chemistry were purchased. The specifications of the pouch batteries used for this study are detailed in Table 3. The cells were 50% discharged when shipped by manufacturers. Because of the lower capacity of the pouch cells, it was considered acceptable to conduct testing on the pouch batteries at 50% SOC vice discharging the batteries to 10% SOC.

Table 3: Specifications of the pouch cells used for testing

Nominal capacity	740 mAh
Nominal voltage	3.7 V
Thickness	5.35 mm
Width	34 mm
Length	59.5 mm
Weight	19 g
Pouch thickness	0.14

The tests conducted on the pouch batteries follow:

- 0.5 inch (12.7mm) Hemispherical punch test
- Vertical Rectangular punch test
- Vertical Cylinder 1.0 inch (25.4mm) diameter punch test
- Conical punch with 0.02 inch (0.51mm) diameter point punch test

Hemispherical punch test

Three separate tests were conducted using the hemispherical punch with a tip radius of 0.5 inches. The punch was attached to the cross head and load cell of the loading frame with a constant velocity of 1.0 mm/min. The test was stopped immediately after the failure occurred.

Figure 18 shows the measured force and displacement variations over time for the three tests performed on the pouch batteries. This figure shows complete reproducibility in terms of shape of the curve as well as the point of drop in force and mechanical failure of the cell. The peak force and associated displacements for the three tests are shown in Table 4. Figure 19 shows the point of short circuit of the cell detected by drop in force and voltage, as well as increase in temperature. One can see from this figure that the peak force and drop in voltage occurs almost simultaneously, all around 180s from the beginning of the test.

Table 4 Force and displacement values at the point of short circuit of the cell

	Peak Force (N)	Displacement (mm)
Test 1	7927.693	2.982
Test 2	7641.984	2.965
Test 3	7605.097	2.947

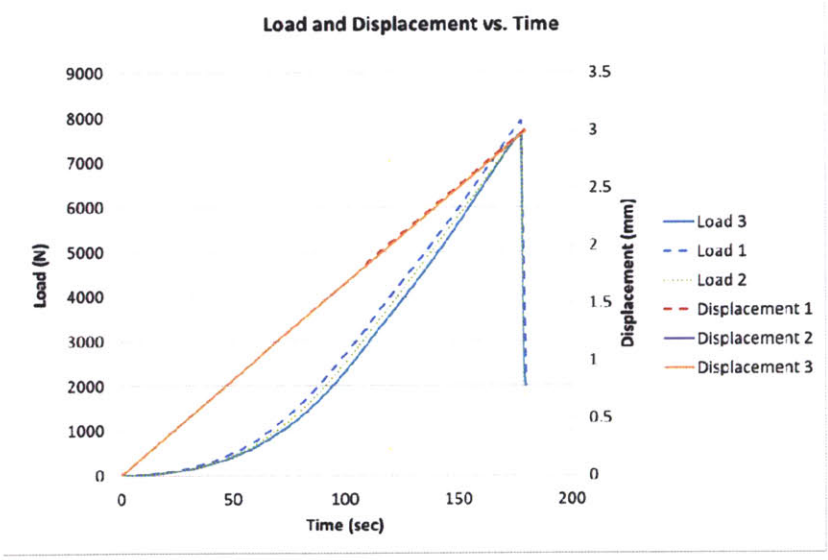

Figure 18: Force and displacement as a function of time for the three punch tests conducted

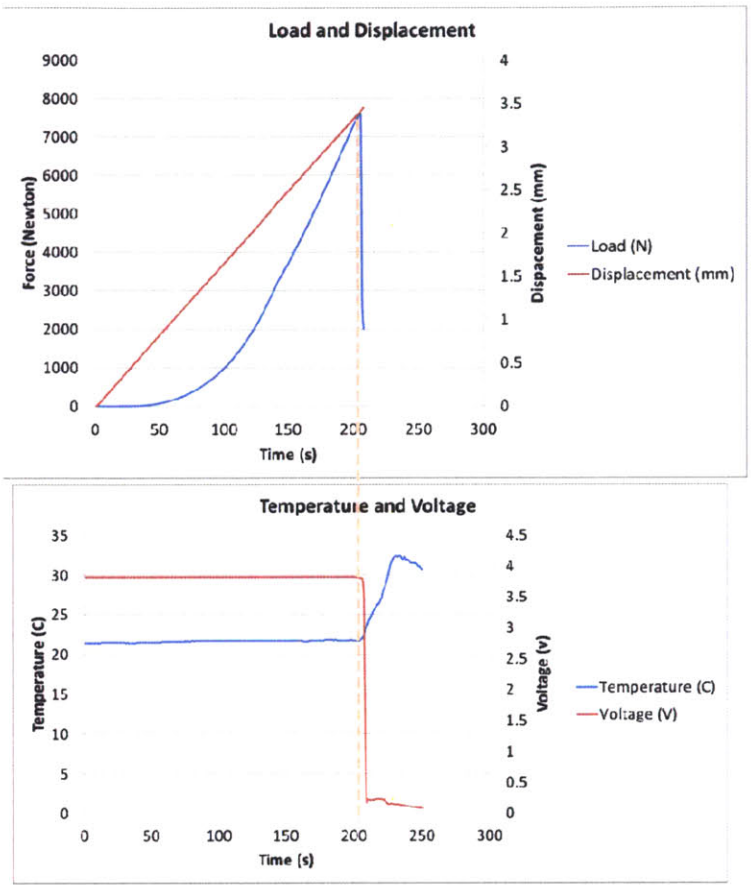

Figure 19: Detecting the point of short circuit from force, voltage, and temperature measurement

Vertical Rectangular Punch Test

The punch with dimensions of 18.2mm x 21.8mm was attached to the cross head and load cell of the loading frame with a constant velocity of 1.0 mm/min. The test was stopped immediately after the failure occurred. Figure 20 (left) shows the point of short circuit of the cell detected by drop in force and voltage, as well as the increase in temperature and Figure 20 (right) shows the punch and resultant cell after testing. Peak force measured was 52845N with an associated displacement of 2.798mm at 168 seconds.

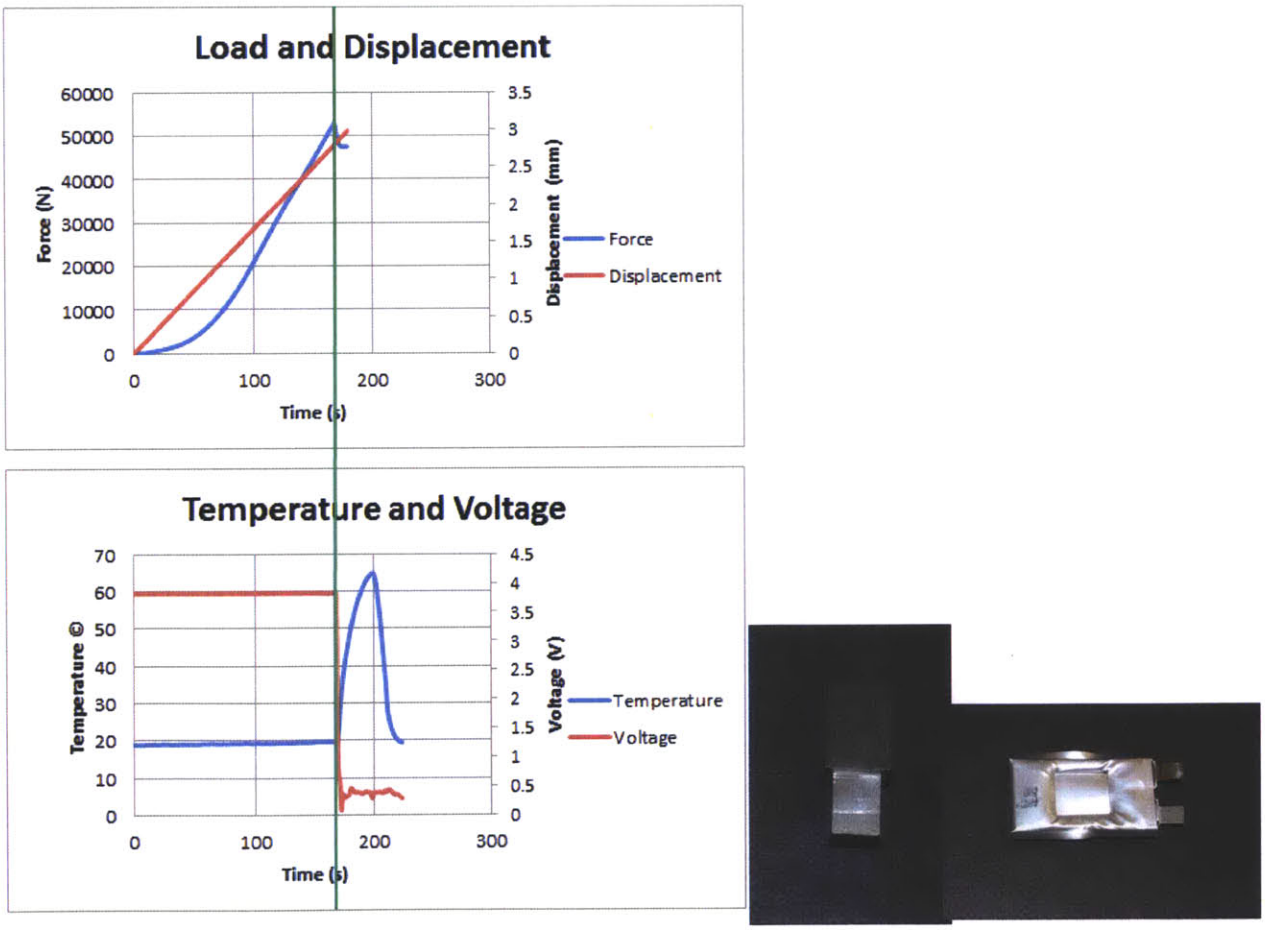

Figure 20: Results of Rectangular Punch Test

Vertical Cylinder Punch Test

The punch was attached to the cross head and load cell of the loading frame with a constant velocity of 1.0 mm/min. The test was stopped immediately after the failure occurred. Figure 21 (left) shows the point of short circuit of the cell detected by drop in force and voltage, as well as increase in temperature and Figure 21 (right) shows the cylindrical punch and resultant cell. Peak force measured was 83870N with an associated displacement of 3.314mm at 199 seconds.

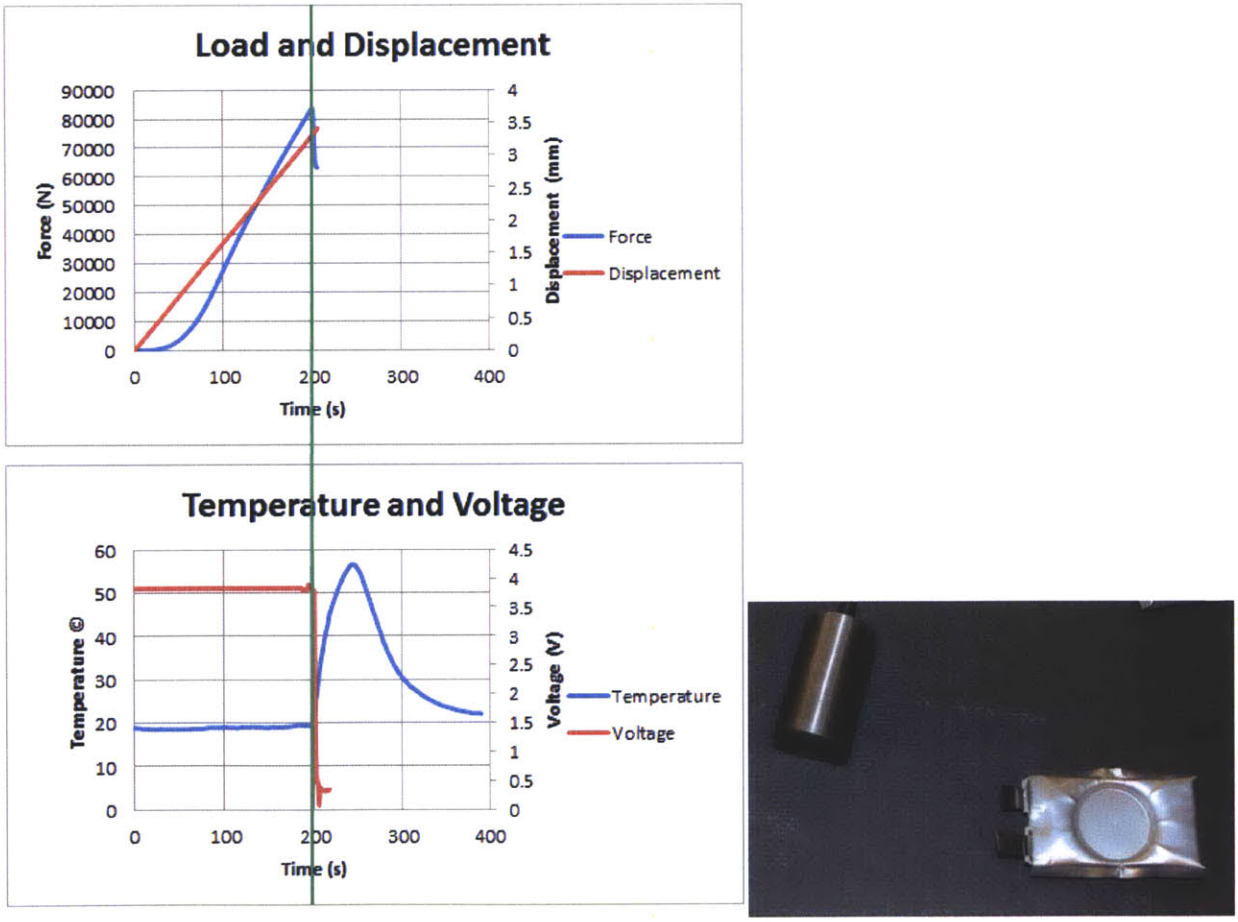

Figure 21: Results of vertical cylindrical punch test

Conical Punch Test

The punch was attached to the cross head and load cell of the loading frame with a constant velocity of 1.0 mm/min. The test was stopped immediately after the failure occurred. XX shows the point of short circuit of the cell detected by drop in force and voltage, as well as increase in temperature. Figure 22 (left) shows the point of short circuit of the cell detected by drop in force and voltage, as well as increase in temperature and Figure 22 (right) shows the conical punch and resultant cell. Peak force measured was 229N with an associated displacement of 1.233mm at 74 seconds.

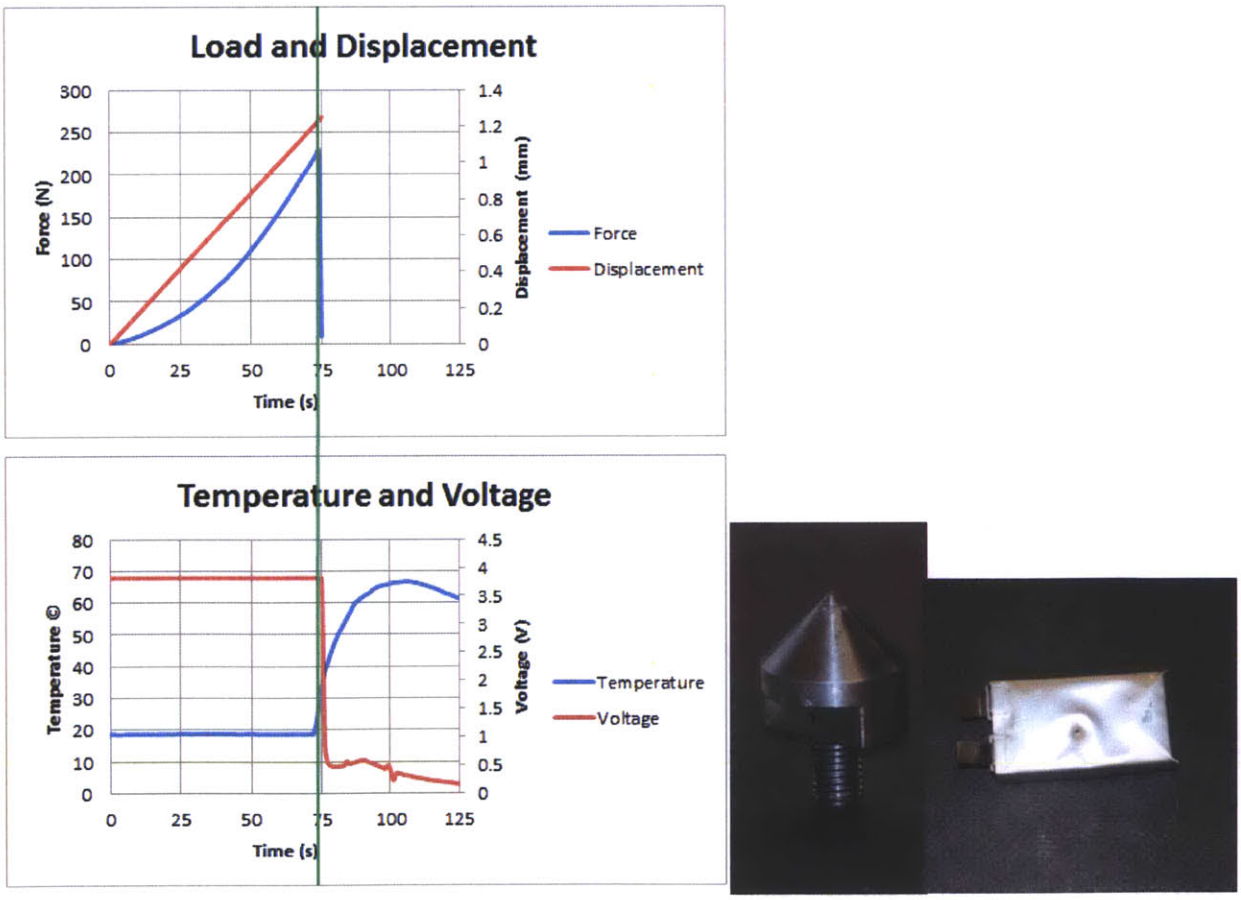

Figure 22: Results of conical punch test

5. Finite Element Analysis Results for 18650 Cylindrical Cells and Pouch/Prismatic Cells

Estimation of Strength of Shell Casing

The crushing strength of a cell comes from both the strength of the outer shell casing and the crush-resistance of the interior core winding. The analysis of the empty shell will provide a quick estimate about the contribution of the shell casing to the overall strength of the entire cell. Closed form solutions of a thin cylindrical shell with and without end caps exist in the literature and will be reviewed under two types of loading: lateral indentation by a rigid rod and lateral compression between two plates.

The static and dynamic response of a thin pipe subjected to a rigid punch loading was studied in a series of publications by Wierzbicki et al (19) (20) (21) The solution that would be most useful to the present problem refers to the resistance of the free end cylinder subjected to lateral knife type of loading. The relationship between the indentation force F and the indentation depth δ is given by:

$$F_{shell} = \sigma_0 t^{1.5} \sqrt{2\pi\delta}$$

Equation 2

where σ_0 is the average flow stress of the material of the shell casing, which was determined in the previous section and t is the thickness of the shell. The above equation is valid in the range of the punch travel not greater than the radius of the shell. It should be noted that the radius of the cylinder does not enter in. The accuracy of the above solution was shown in the literature to compare well with full scale and component tests of pipes subjected to wedge type of loading.

Considering this solution, the contribution of shell casing of the 18650 cell to the total force in a rigid rod indentation scenario is less than one percent (0.25 KN) as compared to the force generated by the local indentation of a cell by a cylindrical rod (see Figure 12) .

The second problem of interest to this study is lateral crushing of an empty tube with end caps removed between two rigid plates. We adopt here a very realistic closed form solution of this problem derived by Runtz and Hodge (22). The crushing force is related to the crush distance through the following equation:

$$F_{yshell} = \sigma_0 t^2 (\frac{L}{R}) \frac{1}{\sqrt{(1-(\frac{\delta}{R})^2)}}$$

Equation 3

where l and R are the length and radius of the battery, respectively. Considering the above simple closed form solution, the shell casing accounts again for less than one percent (0.1 KN) of the resistance of the cell when compressed between two flat plates. It can be concluded that the force generated by the empty outside casing is more than two order of magnitude smaller than the total resistance of the cell under this two loading condition. At the same time, noted the outside casing is important for containing the jelly roll in its designated shape, which will be the case for three-point bending.

Constitutive Model of the Pouch and Jelly Roll

In the case of pouch batteries, the lateral compression of the cell results in a uniform state of stress and strain. Therefore, it is relatively simple to drive the stress strain curve from the load displacement curve. For the cylindrical cells the stress and strain states are highly non-uniform

and change during the loading process. In this paper a homogenized model of the jelly roll is adopted, in which the contribution of all components of the interior of the battery is lumped together into a single type of material. In other words, in this model, it is not intended to quantify the contribution of individual components of the jelly roll. It is recognized that compressive and tensile properties of this material are different. The stress-strain curve obtained for pouch cells in compression is shown in **Error! Reference source not found.**. A simple fit of that measured curve is a parabola:

$$\sigma = B\epsilon^2$$

Equation 4

where B=550 MPa. It should be noted that the active material in pouch batteries tested earlier in the laboratory environment and in the present cylindrical cells are $LiCoO_2$ (cathode) and graphite (anode). Considering that about 80% of the volume of the cell is filled by active material, it is assumed that stress-strain curve determined for pouch batteries could also be used for the present cylindrical cells. The validity of this assumption will be checked by comparing results of simulations with such material input to the experiments explained in Sections 3 and 4. In the numerical simulation, either an analytical fit, Equation 4 or the actual measured curve could be introduced.

In tension, there is a complicated process of failure which could be captured by introducing a cut-off value for the tensile strength. This value controls the onset of short-circuit. In the present paper, the magnitude of tensile cut-off was calibrated from the rigid-rod indentation test, and then validated against the hemispherical punch test. The value of tensile cut off was determined

to be $\sigma_{TC} = 10\ MPa$. According to the present model, when the tensile stress in a representative volume element reaches the cut-off value, it is held constant for the rest of the simulation, see Figure 23.

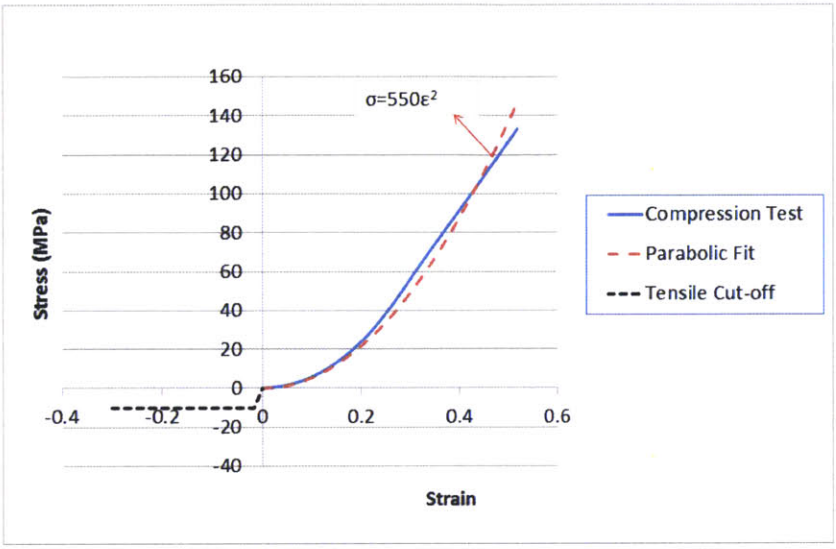

Figure 23: Experimental stress-strain curve, from uniaxial compression of pouch cells with similar chemistry

A finite element model of the cell was developed in LS Dyna software. The shell casing of the cell was discretized using 4-node fully integrated shell elements. The jelly roll was modeled by fully integrated solid elements. The rigid rod/punch and rigid plates were modeled using contact entity from LS Dyna contacts, which assumes a rigid geometrical shape for the contact surface. There were 11167 shell elements and 29106 solid elements in the model. The size of the shell and solid elements were approximately the same (0.8mm). Material piecewise linear plasticity from library of LS Dyna materials was used for the shell casing. The following input was used for the steel shell casing: E=200 GPa, ν=0.3, and σ_{yield}=450 MPa. The effective stress versus

effective plastic strain curve was input to the model from the dog-bone specimen test. The combined shell and solid model is shown in Figure 24.

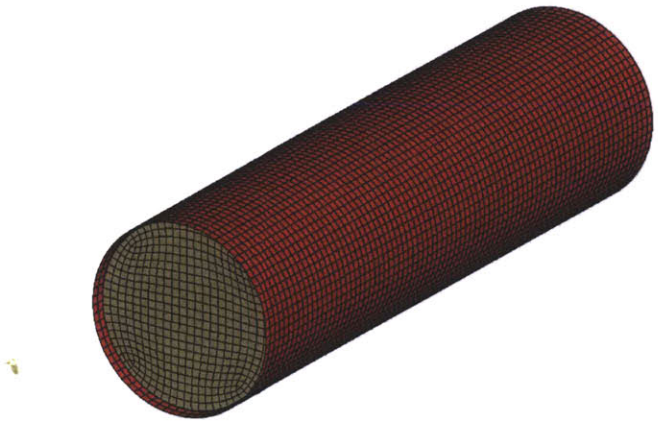

Figure 24: Finite Element Model of the Jelly Roll and Shell Casing

For the jelly roll, the material crushable foam from library of LS Dyna was used. The stress-strain curve shown in Figure 23 was used as the input to all finite element simulations. The rational for choosing this model is that it is consistent with our experimental observation. First, the stress–strain curve obtained from compression test on pouch batteries exhibits a concave shape, which is characteristic for compressible foam with a very low plateau stress. Secondly, this foam model admits different properties in tension and compression. Specifically, the response in tension is elastic with limit on tensile strength, which is referred to as a "cut-off" value. The cut-off stress is determined by inverse method, by performing simulation to match the onset of failure in the rigid-rod indentation test, $\sigma_f = 10$ MPa. The Young modulus could be either introduced as an input number or will be calculated from the stress-strain curve in compression. The maximum slope of the input compression curve is then compared with the value introduced as an independent input, and the largest of two is taken. For present model, the

Young modulus was 500 MPa. Using 8 CPUs to run the simulation, the indentation simulation took approximately 2 hours and 28 minutes, for a relatively small mesh size (0.8 mm in length).

Validation of the model

Three loading scenarios were simulated to validate the material model by comparing the experimentally measured and simulated load displacement curve. This includes indentation by a rigid rod, hemispherical punch crush, and three-point bending.

Indentation by a rigid rod

Figure 25 shows the comparison of rigid rod indentation simulation with the test. It can be observed that the model was able to predict the load- displacement relationship of the cell through the indentation with a very good accuracy. The model also detects the onset of short circuit by the point of a local drop in the force. The point of short circuit in the test occurred at a force level of 6469 N and displacement of 6.3 mm. In the simulation, the peak force is 6532 N at 6.6 mm of deformation. It was observed in experiments that voltage and temperature measurements also verify a short circuit at this point.

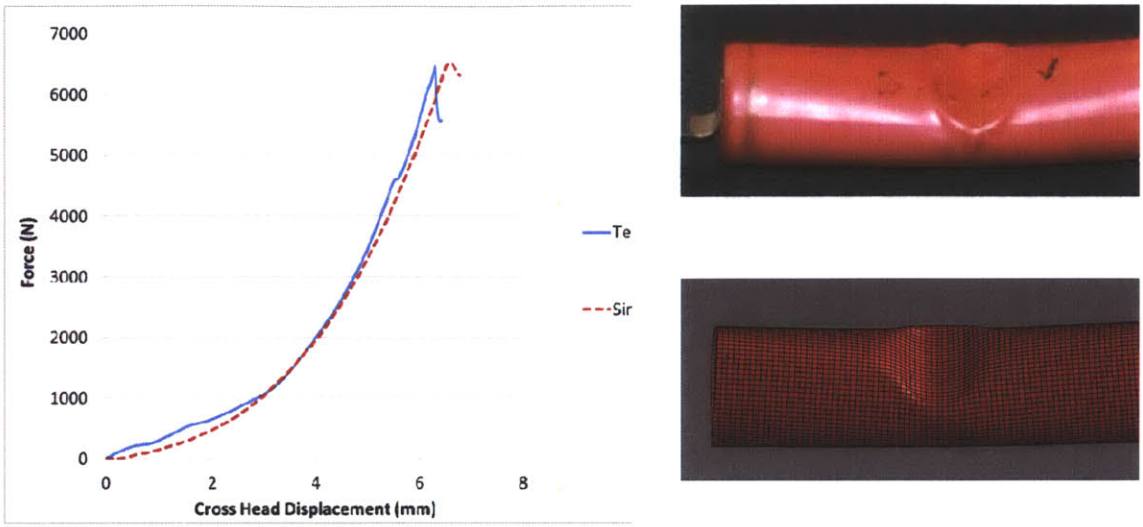

Figure 25: Rigid rod indentation test versus simulation

Location of failure (assumes short-circuit) is detected as the first point reaching a principal tensile stress of 10 MPa, see Figure 26. The short circuit was found to be in the intersection of two planes of symmetry of the cell, at the depth of 4 mm under the punch.

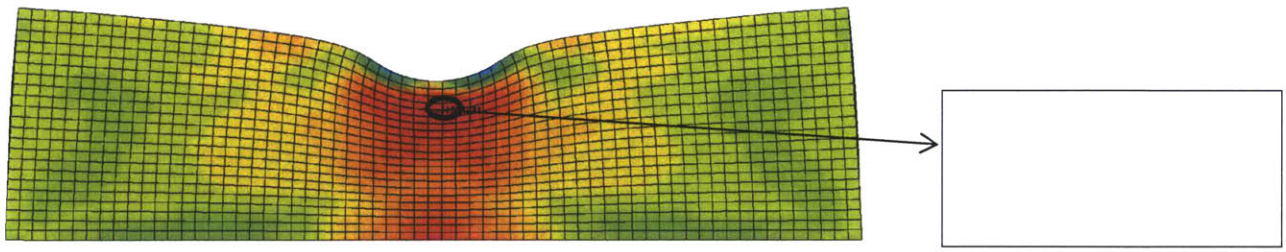

Figure 26: Location of short circuit, Contour of 1st principal stress, rigid rod indentation

Hemispherical Punch Crush

Figure 27 shows the simulation of hemispherical punch crush. Again, it can be observed that the model closely follow the experimental force-displacement of the cell. Model also detects the

onset of short circuit which is evident from drop in force. The measured peak force was 5681 N at 7.3 mm. The values predicted from the simulation were 5647 N and 6.9 mm. It should be noted that the agreement between theory and simulation for the rigid rod indentation was perfect while in the case of spherical punch indentation, the calculated curve is slightly higher than the experimental one. This was to be expected from the model, in which the difference of anisotropic properties in the axial and hoop direction is not accounted for. Still, the error in predicted force is less than 1%.

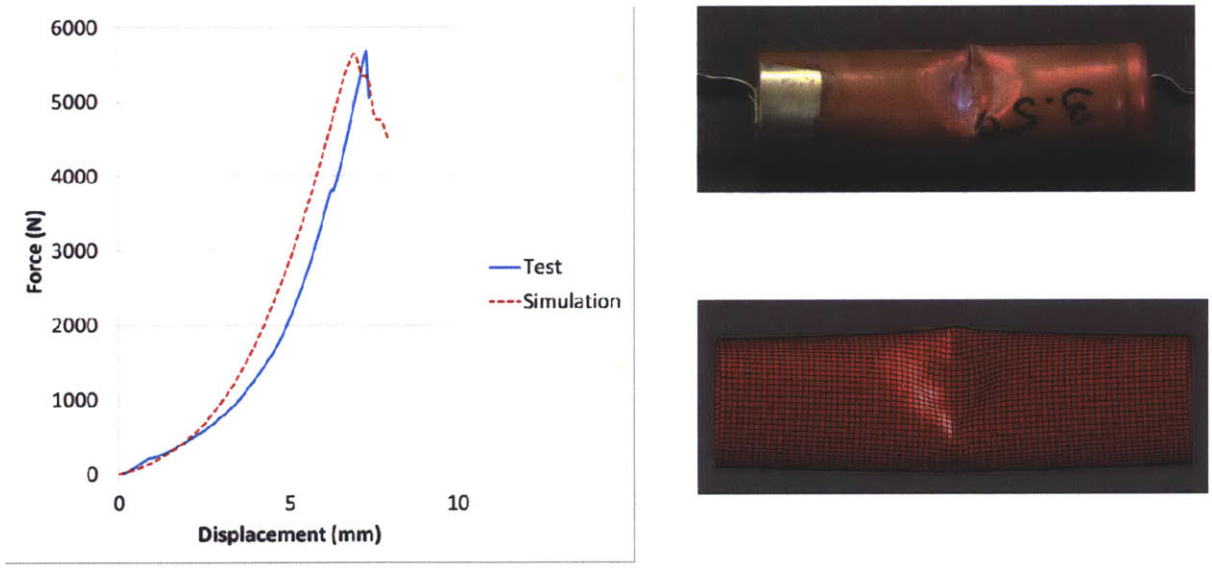

Figure 27 Comparison of tests and simulation for the hemispherical punch crush loading

Location of short circuit is detected as the first point with a tensile principal stress of 10 MPa, see Figure 28. As before, failure (short-circuit) occurs at a location under the punch with identical depth as rigid rod indentation test.

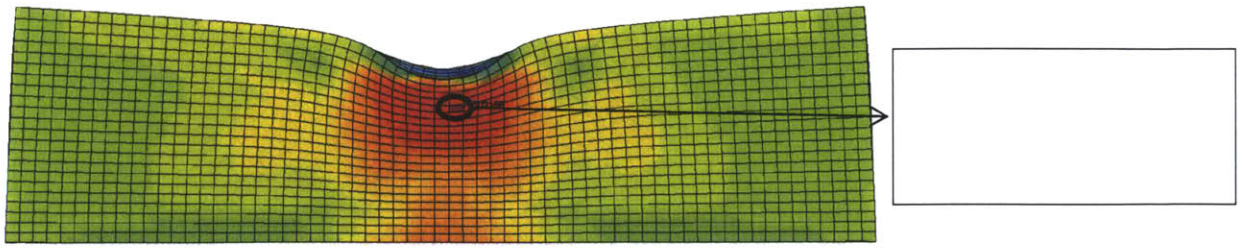

Figure 28: Contour of 1st principal stress, hemispherical punch crush

Three Point Bending Simulation

The three-point bending simulation predicted closely the initial force-displacement relationship and formation of a fold in shell casing under the punch. In particular, the error in prediction of the peak force is about 2%. Shortly after that a progressive fracture of shell casing caused a significant reduction in the strength of the cell. Tensile principal stresses in the jelly-roll rose to a value of 9.9 MPa, which is very close to the cut-off value of 10 MPa , considered as an indicator of short circuit. The above small discrepancy could be caused by asymmetry in load application during the test, because it was very difficult to position the cell at the axis of symmetry of the fixture. At the same time, simulation predicted quite accurately the length of the crack as seen from the comparison shown in Figure 29.

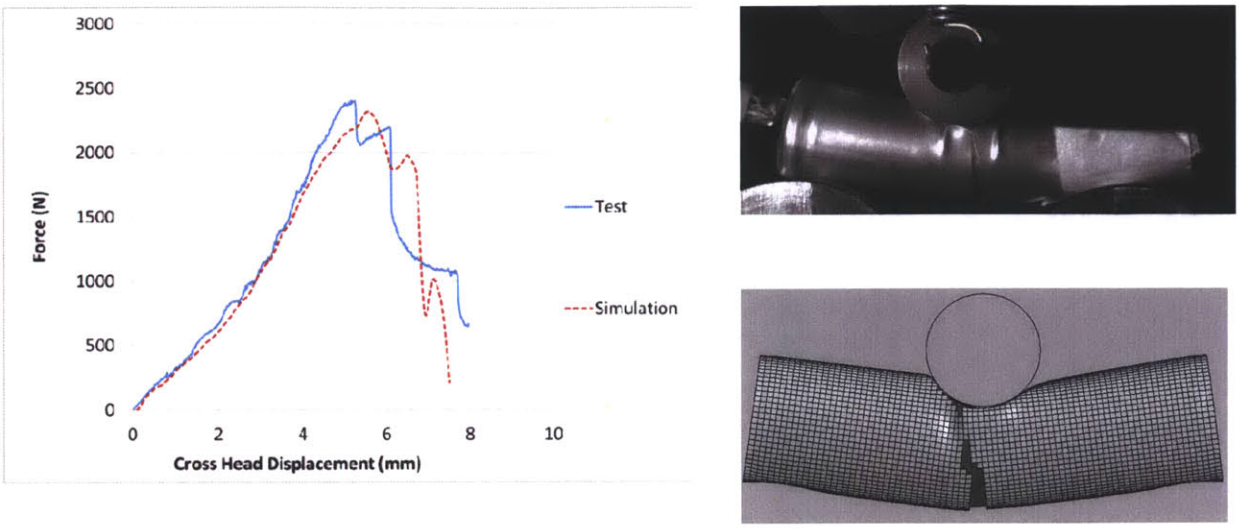

Figure 29 Comparison of Force-Displacement in three-point bending (left), and the shape of the deformed cell (right)

Hemispherical Punch Test on Pouch Cell

The finite element used for this study is a homogenized solid element only model of the pouch cell, developed in LS Dyna software, with 10 elements through the thickness. The assembly of the cell, consisting of anodes, cathodes, and separator has different properties in tension and compression. The compressive stress-volumetric strain for the crushable foam material model was extracted from crushing of the cell between two flat platens as explained in Sahraei et al (2012) (23). The original material model represented the actual cell very closely in the scenario of compression between two flat plates, as shown in Figure 30. The original model cannot predict the point of short circuit correctly, because the tensile properties of the jelly roll were taken from available data in the literature and was not calibrated against testing, see Figure 31.

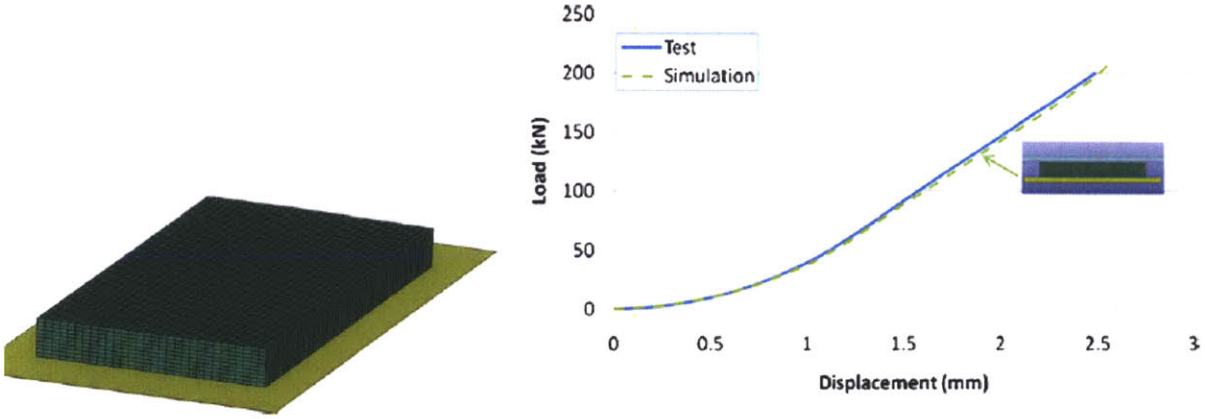

Figure 30: Crushable foam model predicting the load displacement, compression between two plates (20)

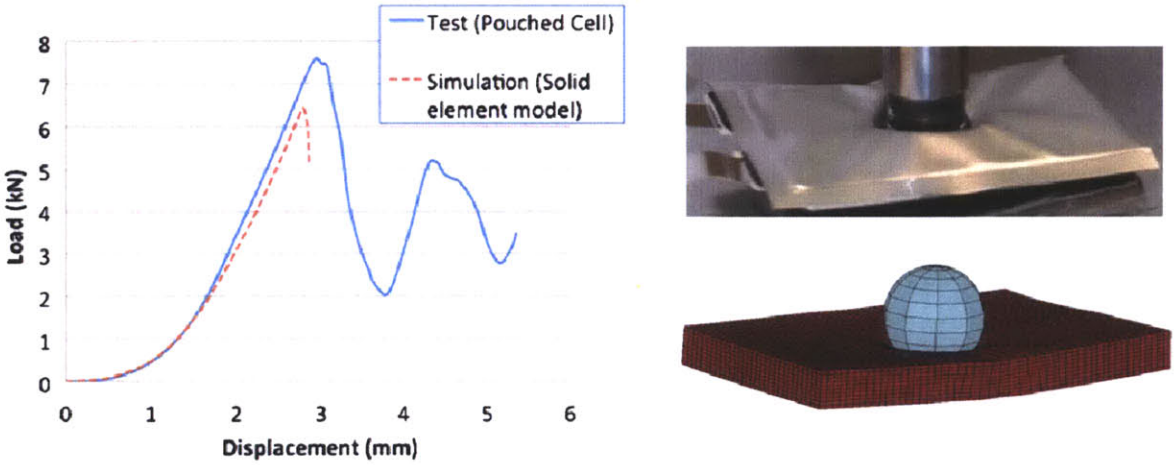

Figure 31: The original model under predicting the onset of short circuit (20)

In this research, we proposed a rigorous calibration method by matching the measured and calculated critical displacement to the peak force. It was found that in order to get a good prediction; the original tensile cut-off value of 56MPa should be increased to 90MPa. With this value and previously determined compressive properties, the present computational model predicts exactly the point of failure, and possible short circuit of the cell, see Figure 32. The predicted peak force increases from 6434 N in the original model, reported in (24), to 7433 N in

the current model. This new value is very close to the maximum load of 7605 N which was achieved during the test shown in Figure 32, giving an error of 2%.

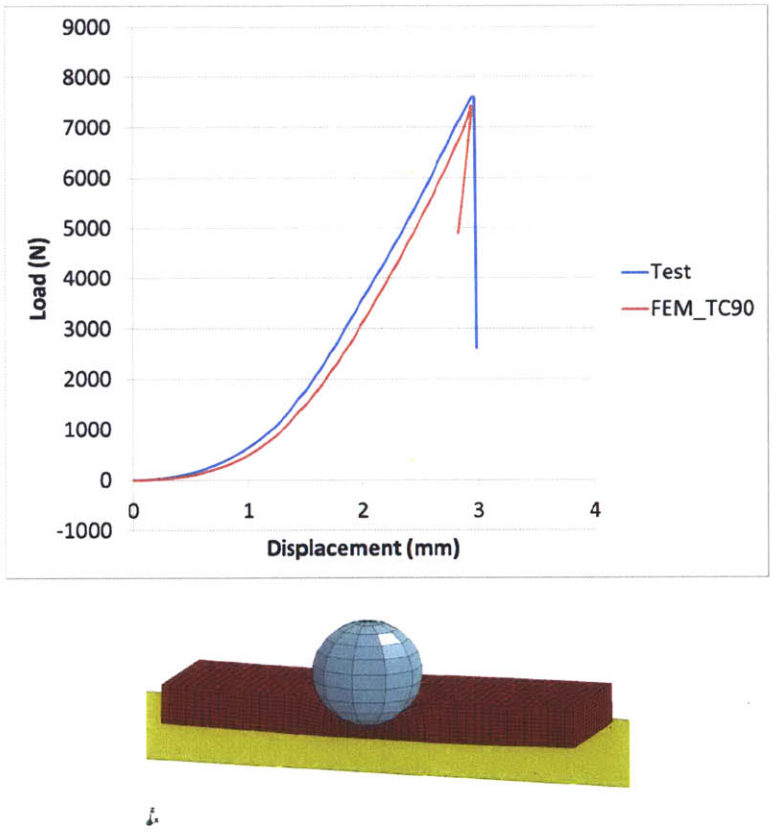

Figure 32 Comparison of Load Displacement curve between the updated FEM simulation and Test no.3 (left), Cross section of cell model at point of maximum deformation (right)

6. Sensitivity Analysis for Cylindrical and Pouch Cells

A series of tests using various diameter rod indentations for the cylindrical cells and various diameter hemispherical punches for the pouch cells was conducted. Table 5 below annotates the rod indentation diameters and peak forces obtained for the cylindrical cells. Table 6 below annotates the hemispherical punch diameters and peak forces obtained for the pouch cells.

Table 5: Cylindrical Sensitivity Analysis Data

Diameter (mm)	Force (N)	Disp (mm)
19.05	5018.68	7.528
28.575	5626.05	6.747
38.1	7940.51	8.099
47.625	8507.67	7.447

Table 6: Hemispherical Sensitivity Analysis Data

Diameter (mm)	Force (N)	Disp (mm)
0.51	229.06	1.23
12.70	7927.69	2.98
28.58	20472.22	4.15
44.45	35199.14	3.40
88.90	64157.32	3.59

It can be inferred that there is a distinct linear correlation between the diameter of the hemispherical punch and the peak force measured. Figure 33 shows this linear correlation and Equation 5 is the linear correlation.

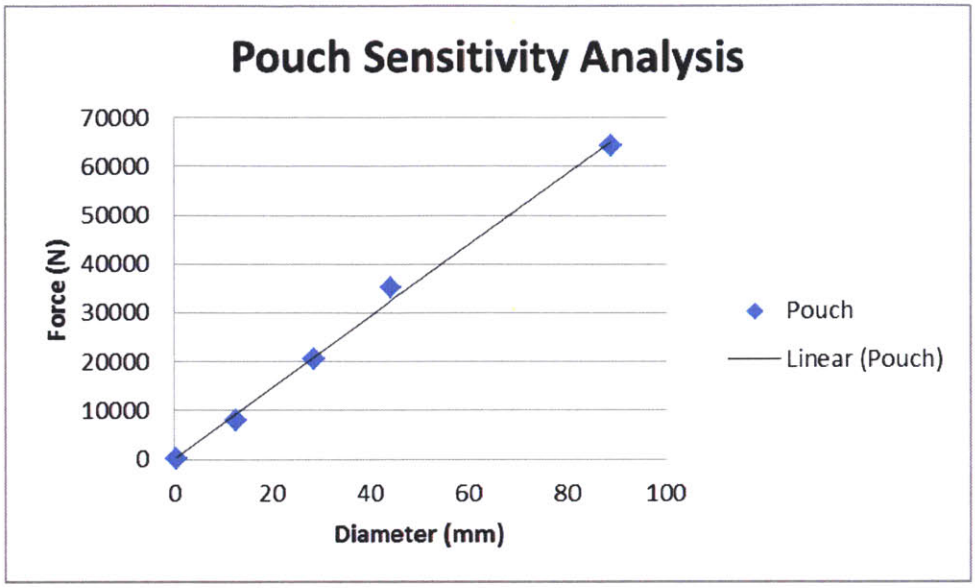

Figure 33: Pouch sensitivity analysis

Equation 5: Linear interpolation for pouch cells

There is a loose linear correlation between the diameters of the rods used for the cylindrical cell tests and the peak force. It is believed that damage occurred to the 10KN load cell generating a bias in the measured peak forces. Figure 34 is included for informational purposes only along with Equation 6. It is expected that the intercept of Equation 6 will not go to zero, because of the steel casing surrounding the cell and the jelly roll material having inherent strength resisting fracture due to an applied load. The interpolated bias (y-intercept) of 2299.7 N is well above the expected values of approximately 2% of fracture loading.

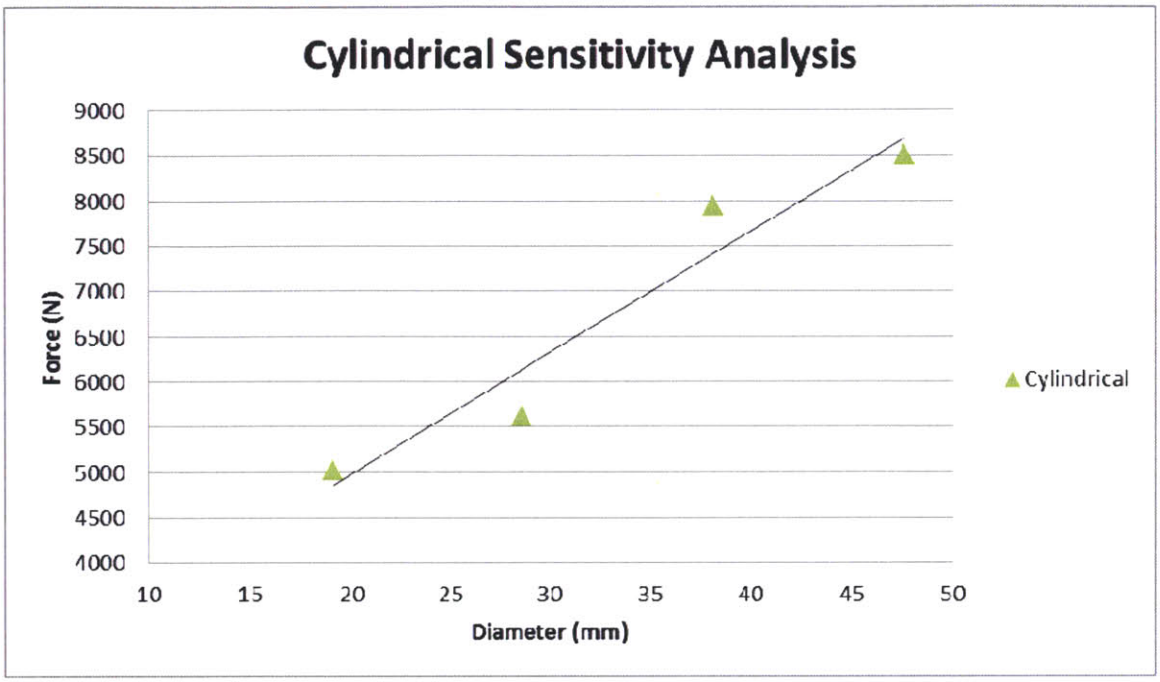

Figure 34: Cylindrical sensitivity analysis

Equation 6: Linear interpolation for cylindrical cells

7. Conclusions and Recommendations

From this continuing experimental and computational study, the following conclusions can be drawn from both the data and the simulations:

(i) Pouched or prismatic batteries, although volumetrically more efficient, require significantly more structural support than cylindrical cells. The casing on the prismatic cells is of a plastic-aluminum construction and the cylindrical cells are a steel housing. Additionally the shape of the cylindrical cell, by nature is inherently stronger than the pouched cell.

(ii) Because of the correlation between cell voltage cutoff and a rapid temperature increase at the internal fracture point of force, it has been shown that a computational model can accurately predict internal short circuit in mechanical abuse situations.

(iii) There is a linear relationship between the peak forces measured using the various sized punches and rods in testing and the size of the rod or punch. This linear relationship helps to simplify the homogeneous nature of the computational model.

(iv) In development of the constitutive model it is noted that the tensile cutoff was the most important and key parameter in calibrating the model to the laboratory tests.

The MIT Battery Consortium, in conjunction with the Crashworthiness Lab, will continue to develop and refine the constitutive model to make it flexible for future battery chemistries and construction techniques with minimal laboratory testing. The model will have a variable to allow for adjustments to the tensile cutoff set point for future cell developments.

The cells tested in the Crashworthiness Lab were discharged to 50% SOC for the small pouch cells and 90% for the cylindrical 18650 cells. Because the testing was only done at one SOC, additional refinement of the model may be necessary for other SOC levels.

Additionally, the constitutive model will be integrated into existing crash testing software in order to accurately model the behavior of a battery pack in a modeled vehicle during a collision event.

References

1. *Lithium-Ion Batteries for Autonomous Underwater Vehicles.* **Raman, N.S., Briscoe, J. Douglass, Grivel, Tristan.** 2002.

2. **Fischetti, Mark.** Charge under Control. *Scientific American.* 2010, Vol. 303, pp. 26-27.

3. **Commander, Naval Ordnance Center.** *Technical Manual for Navy Lithium Battery Safety Program Responsibilities and Procedures.* s.l. : Naval Sea Systems Command, 2010.

4. **Commander, Naval Seas Systems Command.** *High-Energy Storage System Safety Manual.* s.l. : Naval Sea Systems Command, 2011.

5. **Juzkow, Mark W., Mayer, Steven T.** *Design Considerations for Lithium-ion Cells Part I: Cell Components.* PolyStor Corporation. Dublin, CA : IEEE, 1997.

6. **Juzkow, Marc W., Mayer, Steven T.** *Design Considerations for Lithium-ion Cells.* PolyStor Corporation. Dublin, CA : IEEE, 1997.

7. Electropaedia. *http://www.mpoweruk.com/cell_construction.htm.* [Online] Woodbank Communications Ltd., 2005.

8. *Mechanical behavior of battery separator in electrolyte solutions.* **Sheidaei, Azadeh, Xiao, Xinran, Huang, Xiaosong, Hitt, Jonathon.** 2011, Journal of Power Sources, Vol. 196, pp. 8728-8734.

9. *Joining Technologies For Automotive Lithium-Ion Battery Manufacturing - A Review.* **Shawn Lee, S., Kim, Tae H., Jack Hu, S., Cai, Wayne W., Abell, Jeffrey A.** Erie, PA : ASME, 2010.

10. **Wang, Qingsong, Ping Ping, Sun, Jinjua.** Catastrophe analysis of cylindrical lithium ion battery. *Nonlinear Dynamics.* 2010, Vol. 61, pp. 763-772.

11. **Swart, Jan, Slee, Daren.** *Failure Analysis Methodology for Battery Powered Product Incidents.* Phoenix, AZ : IEEE, 2008.

12. *Safety mechanisms in lithium-ion batteries.* **Balakrishnan, P.G., Ramesh, R., Prem Kumar, T.** 2006, Journal of Power Sources, Vol. 155, pp. 401-414.

13. *Lithium ion cell safety.* **Toboshima, Shin-ichi, Takei, Koji, Sakurai, Yoji, Yamaki, Jun-ichi.** 2000, Journal of Power Sources, Vol. 90, pp. 188-195.

14. **Berdichevsky, Gene, Kelty, Kurt, Straubel, JB, Toomre, Erik.** *The Tesla Roadster Battery System.* s.l. : Tesla Motors, 2006.

15. *Vehicle integration issues for hybrid energy storage systems.* **Guerin, J.T., Leutheuser, Andrew.** 2010, International Journal of Energy Research, Vol. 34, pp. 164-170.

16. **Sun, Fengchun, Hu, Xiaosong, Zou, Yuan, Li, Siguang.** Adaptive unscented Kalman filtering for state of charge estimation of a lithium-ion battery for electric vehicles. *Energy.* 36, 2011, pp. 3531-3540.

17. *Abuse behavior of high-power, lithium-ion cells.* **Spotnitza, *, Franklin J.** 2009.

18. **Shriram.** *Analysis of Internal short-circuit.* 2009.

19. *Indentation of tubes under combined loading.* **Wirzbicki T., Suh MS.** 3 / 4, 1988, International Journal of Mechanical Sciences, Vol. 30, pp. 229-248.

20. *Damage of plastic cylinders under localized pressure loading.* **Hoo Fatt M., Wierzbicki T.** 12, 1991, International Journal of Mechanical Sciences, Vol. 33, pp. 999-1016.

21. *Industrial fracture consortium.* **Wierzbicki T., Mohr, D.** s.l. : MIT, January 2011 - December 2013.

22. *Crushing of tubes between rigid plates.* **De Runtz J. A., Hodge, P. G.** 1963, Journal of Applied Mechanics, Vol. 30, pp. 381-395.

23. **Sahraei, Elham, Hill, Rich, Wierzbicki, Tomasz.** Calibration and finite element simulation of pouch lithium-ion batteries for mechanical integrity. *Journal of Power Sources.* 2012, 201, pp. 307-321.

24. **Sinz, Wolfgang et al.** Integration of a crashworthy battery in a fully electric city bus. *International Journal of Crashworthiness.* 2011.